Texture and geochemistry of sphalerite from the Chitudian Pb-Zn-Ag deposit, southern margin of the North China Craton: Implications for the enrichments of Cd, Ga, and In

Cheng Chen [a,b,c], Lei Meng [d], Jing Xu [e], Qiang Zhan [a,b,c], Taiping Zhao [a,b,*]

[a] Key Laboratory of Mineralogy and Metallogeny, Guangzhou Institute of Geochemistry, Chinese Academy of Sciences, Guangzhou 510640, China
[b] CAS Center for Excellence in Deep Earth Science, Guangzhou 510640, China
[c] University of Chinese Academy of Sciences, Beijing 100049, China
[d] State Key Laboratory of Ore Deposit Geochemistry, Institute of Geochemistry, Chinese Academy of Sciences, Guiyang 550081, China
[e] Zijin School of Geology and Mining, Fuzhou University, Fuzhou 350108, China

ARTICLE INFO

ABSTRACT

The Chitudian Pb-Zn-Ag deposit, located in the southern margin of the North China Craton (SNCC), is a typical magmatic-hydrothermal deposit, where sphalerite is the predominate ore mineral with significant concentrations of critical metals, including Ga, In, and Cd. However, previous studies paid little attention to the critical metals in the deposit. This study carried out in-suit elemental analysis on the sphalerite from the Chitudian deposit, aiming to constrain the spatial distribution and enrichment mechanism of critical metals. In the Chitudian deposit, five types of sphalerite were identified (Z-Sp, Y-Sp1, Y-Sp2, X-Sp1, and X-Sp2), which differ in color, texture, and chemical composition. The concentrations of Cd, Ga, and In of these sphalerites range from 1440 to 5145 ppm, 0.53 to 528 ppm, and 0.75 to 2113 ppm, respectively. In detail, Cd is mainly concentrated in the sphalerites from the hydrothermal vein-type orebodies relative to skarn-type orebodies. Indium is progressively depleted from granite-proximal locations to granite-distal locations, and the Fe-rich sphalerite is an excellent host of In. Gallium enrichment is only observed in the tectonically deformed location of the sulfide ore vein, where the Ga-rich sphalerite is poor in Fe and shows a complex texture. Microanalysis conducted on the Ga-rich sphalerite suggested that Ga, together with In, Sn, and Cu, are removed from the deformed sphalerite by mineral-fluid interaction and subsequently sequestered by the late sphalerite cement. Considering that the Ga-rich sphalerite is close to the Ga-bearing coal bed of the Meiyaogou Formation, it is likely that the coal bed could be a potential source for Ga. These results highlight that tectonic deformation followed by hydrothermal fluid overprinting is favorable for the enrichment of critical metals in sphalerite-rich deposits.

1. Introduction

Critical metals such as Ga, Ge, Cd, and In have irreplaceable and significant applications in emerging industries, e.g., new materials, "green" technologies, and information technologies (Werner et al., 2017; European Commission, 2019). Due to their low abundance in continental crust, it is difficult to concentrate in large amounts, and there is no deposit dominated by Ga-, Ge-, Cd-, or In-minerals (Rudnick and Gao, 2014; Wen et al., 2019). Generally, these metals are associated with sphalerite-rich deposits, and most of them are extracted from zinc concentrates as byproducts (Frenzel et al., 2014; Werner et al., 2017; Mondillo et al., 2018a). Numerous studies have shown that the

enrichment of In dominantly occurs in high-temperature Zn deposits formed in magmatic-hydrothermal systems, whereas Ga, Ge, and Cd tend to enrich in low-temperature Zn deposits without obvious magmatic contributions (Zhang et al., 1998; Murakami and Ishihara, 2013; Belissont et al., 2014; Frenzel et al., 2016). Specifically, In is mainly derived from the granite-related Sn-Zn deposits, while Ga, Ge, and Cd are sourced from the MVT (Mississippi Valley-Type) or SEDEX (Sedimentary Exhalative) Pb-Zn deposits (Zhang, 1987; Cugerone et al., 2018; Wei et al., 2019; Wen et al., 2019; Zhao et al., 2022).

Recent work has demonstrated that the base-metal sulfide deposits formed in porphyry Cu/Mo systems have a great resource potential for critical metals such as Re, In, Ge, Ga, Se, and Te (John and Taylor, 2016;

Sahlström et al., 2017; Benites et al., 2021; Stergiou et al., 2021). The Luanchuan ore district, located on the southern margin of the North China Craton (SNCC) (Fig. 1a-b), is the most important Mo-polymetallic ore district in China for the presence of several large to super-large porphyry-skarn Mo–W deposits, such as Nannihu, Sandaozhuang, Zhongyuku, Shangfanggou, and Huoshenmiao deposits (Fig. 1c) (He et al., 2020; Wang et al., 2021). In the last two decades, numerous Pb–Zn (–Ag) polymetallic veins have been laterally discovered outside the Mo–W deposits (Fig. 1c), and >5 Mt Pb + Zn have been revealed in the Luanchuan ore district (Ye, 2006; Duan et al., 2011; Cao et al., 2015; Yang et al., 2017a). Sphalerite, as one of the most important economic minerals in these Pb–Zn(–Ag) polymetallic veins, has been proven to be a significant host mineral for Cd, Ga, and In (Yin and Hu, 2004; Cao et al., 2013; Tian et al., 2015; Xing et al., 2017). However, previous studies have predominantly focused on the genesis of the Pb–Zn(–Ag) polymetallic veins. The spatial distribution of Cd, Ga, and In and their enrichment mechanism is poorly constrained.

The Chitudian Pb-Zn-Ag deposit, located in the Luanchuan ore district, consists of several Pb-Zn-Ag veins, which are laterally or vertically associated with a concealed porphyry-skarn Mo deposit (Fig. 2). Previous studies suggested that the deposit is a distal product of porphyry Mo system, based on the C-H-O-S-Pb isotope, fluid inclusion, and geochronology data (Cao et al., 2015). Moreover, geochemical data of ore minerals indicated that the Chitudian deposit contains considerable Cd, Ga, and In resources in sphalerite (Cao et al., 2013; Tian et al., 2015), but up to now, there is no research on these critical metals. In this study, we investigate the textures and chemical compositions of different types of sphalerite from the Chitudian Pb-Zn-Ag deposit by using transmitted light, ultraviolet light, back-scattered electron imaging (BSE), electron microprobe analysis (EMPA), and laser ablation-inductively coupled plasma-mass spectrometry (LA-ICP-MS). These integrated datasets presented here give us a better understanding of the enrichments of critical elements in the deposit. Meanwhile, a mechanism was proposed to explain the genesis of the sphalerite with a complex texture and abnormal concentrations of In and Ga.

2. Geological setting

2.1. Regional geology

The SNCC is one of the most important molybdenum polymetallic metallogenic belts worldwide (Mao et al., 2011) and is bound by the Sanmenxia–Lushan Fault to the north and the Luanchuan Fault to the south (Fig. 1). It mainly consists of the Archean to Paleoproterozoic high-grade metamorphic basement variably overlain by the Mesoproterozoic to Late Paleozoic cover sequences (Zhao et al., 2004; Xu et al., 2009). During the Late Mesozoic, the SNCC recorded intensive tectonic-magmatic activity under the background of craton destruction and lithospheric thinning (Gao and Zhao, 2017). The widely distributed granitoids in this region are spatially and temporally associated with the large-scale Mo-W-Pb-Zn-Ag mineralization, including porphyry-skarn Mo-W deposit, skarn Zn(-Pb) deposit, and hydrothermal-vein Pb-Zn-Ag deposit (Mao et al., 2011; Zhao et al., 2018). Numerous studies suggested that different types of deposits in the SNCC were genetically related, and a regional Mo-W-Pb-Zn-Ag mineralization system has been established (Mao et al., 2009; Cao et al., 2015; Jin et al., 2019; Li et al., 2017).

The Luanchuan ore district contains total reserves of 6.31 Mt Mo, 1.38 Mt WO₃, >500 Mt Zn + Pb, and abundant Ag resources (Li et al., 2015; He et al., 2020). Three different types of deposits were identified in this district, including porphyry-skarn type Mo–W deposit, skarn-type Zn(-Pb) deposit, and hydrothermal vein-type Pb-Zn-Ag deposit from granite-proximal location to granite-distal location. Most of these deposits were hosted by the Paleozoic sedimentary rocks belonging to the Guandaokou, Luanchuan, and Taowan Groups (Fig. 1c) (Cao et al., 2015). The Guandaokou Group includes the Baishugou, Fengjiawan,

Duguan, Xunjiansi, Longjiayuan, and Gaoshanhe Formations and consists of dolomitic marble locally interlayered with terrigenous clastic rocks. The Luanchuan Group consists of the Sanchuan, Nannihu, Meiyaogou, Dahongkou, and Yuku Formations from bottom to top, which are mainly composed of clastic sediments, carbonates, and alkaline volcanic rocks. The Taowan Group is divided into three groups, including the Qiumugou, Fengmaimiao, and Sanchakou Formations, which are primarily siltstone, quartzite, phyllite, conglomerate, and argillaceous marble. In the Luanchuan ore district, the Luanchuan and Guandaokou groups are the most widely distributed ore-bearing strata with Mo, W, Pb, Zn, and Ag resources (Yang et al., 2017a, Yang et al., 2017b).

Complex faults and folds are developed in the Luanchuan district (Li, 2014). The regional structures are defined by NWW-striking thrust faults, which are superimposed by subordinate NE-striking strike-slip faults (Fig. 1c). The distribution of granitic plutons and related deposits is controlled by the NWW-trending tectonic systems developed in the Luanchuan Group and Guandaokou Group (Duan et al., 2011; Yang et al., 2017b; Zhang et al., 2019). The Late Jurassic-Early Cretaceous granites (e.g., Nannihu, Huangbeilin, Dongyuku, and Shibaogou), classified as highly differentiated I-type granitoids, are spatiotemporally related to the different types of deposits in this district (Figs. 1 and 2) (Bao et al., 2014; Wang et al., 2018; Xue et al., 2018; Zhang et al., 2018). These small granitic plutons that occurred on the surface were connected to a large concealed granite batholith with a volume of 96.96 km³, which supplied sufficient mineralizing fluids and metals for the polymetallic mineralization (Zhang et al., 2019; He et al., 2020).

2.2. Deposit geology

The Chitudian deposit, approximately 15 km northwest of the Luanchuan County, Henan Province, has proven reserves of 1.69 Mt Pb + Zn and 2407 t Ag (Tian et al, 2015). The exposed strata in the Chitudian deposit comprise the clastic sediments and carbonates belonging to the Luanchuan Group (Fig. 2). As the principal country rock of orebodies, the Meiyaogou and Sanchuan Formation are mainly composed of marble, schist, and quartzite. The magmatic intrusion in this area includes the Huangbeiling (porphyritic monzogranite), Dongyuku (granite porphyry), and Shibaogou (porphyritic monzogranite) granites. Recently, a drilling program conducted in the Huangbeiling-Dongyuku area revealed a concealed granitic batholith (153–130 Ma) and a superlarge concealed Mo-W deposit with a molybdenite Re-Os age of 146 Ma (Li et al., 2015; Guo et al., 2018; Zhang et al., 2019; He et al., 2020; Fig. 2b). According to previous studies, the Chitudian deposit (~137 Ma) was interpreted to be associated with the Mesozoic granites in this district (Cao et al., 2015; Cao et al., 2016).

In the Chitudian deposit, alteration types primarily include skarnization, silicification, and carbonatization. The deposit consists of several sulfide veins that are located at the core and flanks of the Huangbeiling-Shibaogou anticline and controlled by NW-striking faults (Fig. 2). Two types of Pb–Zn–Ag mineralization have been revealed in the Chitudian deposit, including skarn and hydrothermal-vein type mineralization. Field investigation suggested that the hydrothermal-vein type ores are more important than skarn-type ores volumetrically. Numerous studies indicated that these two types of Pb-Zn orebodies and the centered porphyry Mo deposit constitute a unified magmatic-hydrothermal mineralization system, and the skarn-type Pb-Zn orebodies are the proximal product of this system, while the hydrothermal-vein type orebodies are the distal product of this system (Mao et al, 2009; Li et al., 2017; Jin et al., 2019). From proximal skarn-type Pb-Zn orebodies to distal hydrothermal vein-type Pb–Zn–Ag orebodies, the alteration, mineral association, and ore-forming fluid systematically change from high temperatures to low temperatures (Cao et al., 2015; Zhao et al., 2018).

The skarn-type orebodies are represented by S039 and S068 ore veins in the Zhongyuku ore block (ZOB) (Fig. 2), where Zn is the dominant
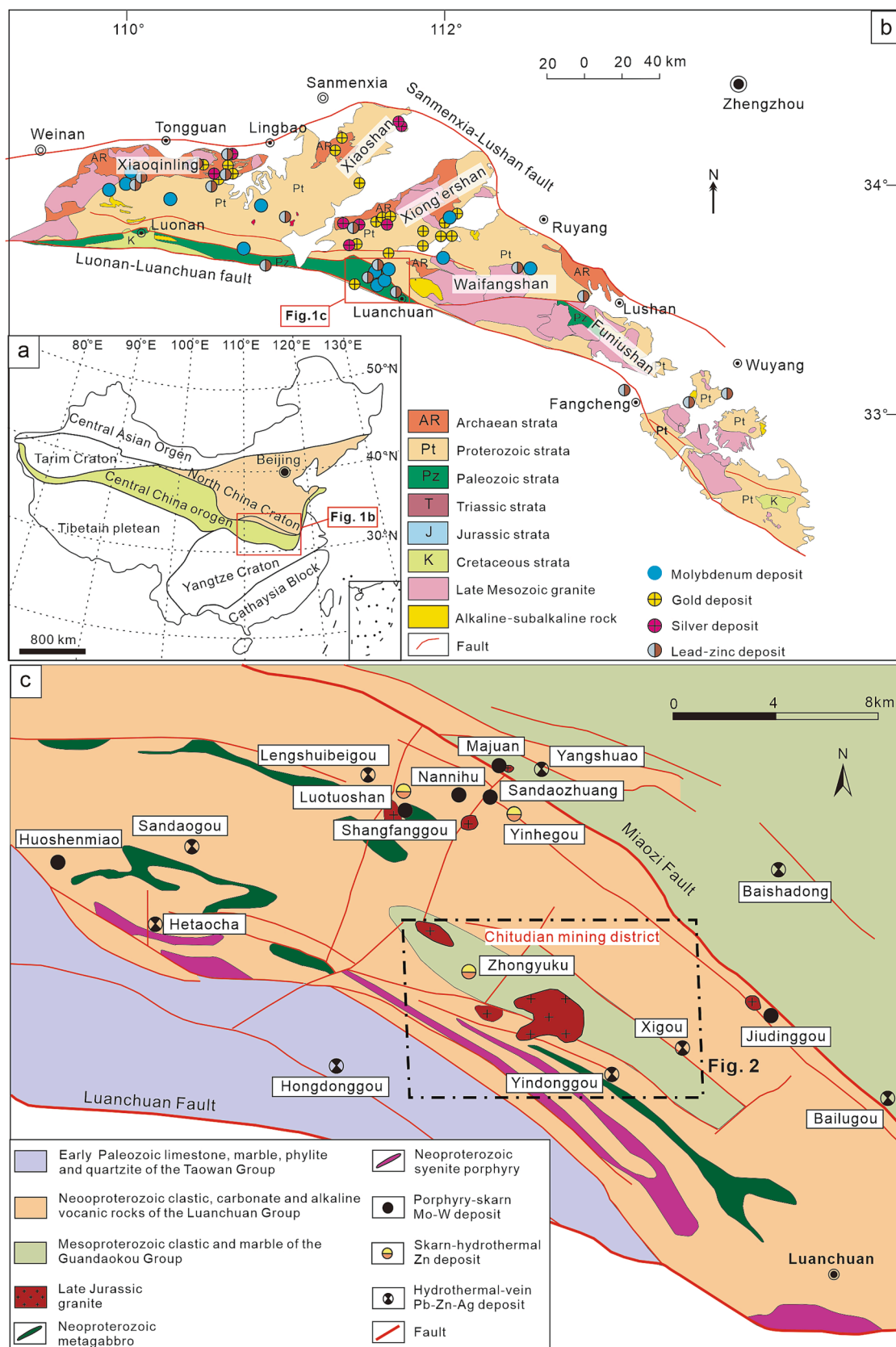
Fig. 1. (a) Tectonic map of China showing the major tectonic units surrounding the North China Craton. (b) Distribution of the deposits in the southern margin of the North China Craton. (c) Distribution of the Mesozoic granitoids and deposits in the Luanchuan ore district. Modified after Mao et al. (2011) and Zhang et al. (1996).
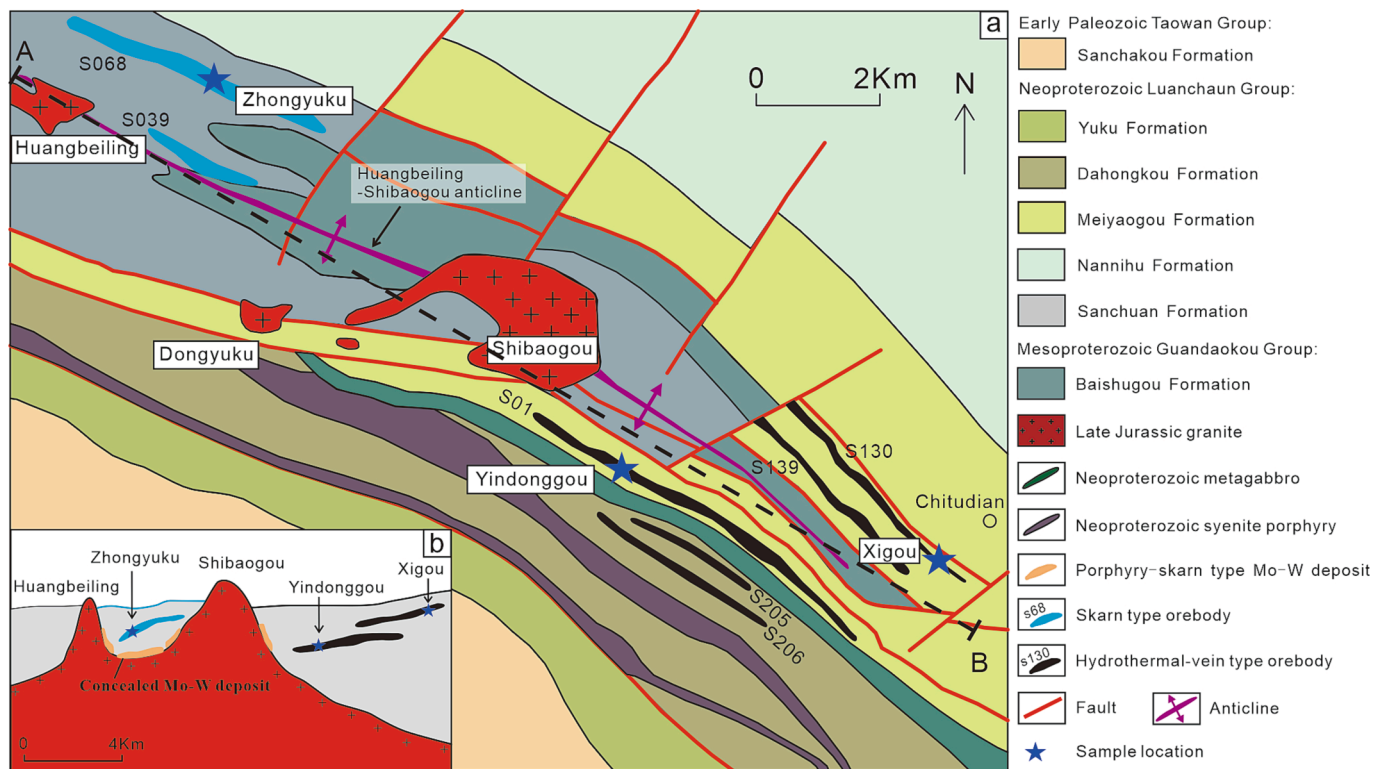
Fig. 2. (a) Geological map of the Chitudian Pb-Zn-Ag deposit (modified after Tian et al. (2015)). (b) A sketch profile showing the spatial relationship between orebodies and granites. The sample locations were projected to this profile.

metal resource at a grade of 1.70–5.73 wt%. Based on cross-cutting relationships and microscopic observations, three alteration-mineralization stages have been recognized. Stage 1 (skarn stage) predominantly consists of garnet and pyroxene, with minor tremolite, wollastonite, and epidote (Fig. 3a). Stage 2 (sulfide stage) is dominated by sulfides, such as sphalerite, pyrrhotite, pyrite, chalcopyrite, and galena (Fig. 3b and Fig. 4a-c). Stage 3 (carbonate stage) is composed of abundant quartz, calcite, and fine-grained pyrite, which crosscuts the early sulfides (Fig. 3c).

The hydrothermal vein-type orebodies are mainly distributed in the west of Shibaogou granite, including S01, S204, and S206 ore veins in the Yindonggou ore block (YOB), and S130 and S139 ore veins in the Xigou ore block (XOB) (Fig. 2). These orebodies are main supplier of Zn, Pb, and Ag resources, with a grade of 4.18–11.38 wt%, 0.40–9.70 wt%, and 18.4–408 ppm, respectively. The mineral assemblages and field investigation indicate that the ore-forming processes can be divided into three stages. Stage 1(calcite-pyrite stage) is characterized by the formation of pyrite, calcite (yellow), and minor quartz (Fig. 3d). Stage 2 (quartz-polymetallic sulfide stage) is marked by sphalerite, galena, pyrite, and arsenopyrite (Fig. 3f-g and 4 g). Stage 3 (quartz-calcite stage) is sulfide-barren, consisting of abundant calcite (white) and quartz (Fig. 3d).

3. Samples and analytical methods

All of the ores, in this study, were sampled from underground mines and surface outcrops of the ZOB (S068), YOB (S01), and XOB (S130). The sample locations shown in Fig. 2 correspond to a proximal to distal position, relative to the concealed granite. Samples from the ZOB are dominantly sphalerite-pyrrhotite-pyrite ores, and those from the YOB and XOB are sphalerite-galena ores. Each sample was first prepared as polished thin section and observed under optical microscope. Then, a total of fifteen representative samples were chosen for scanning electron microscopy (SEM) analysis, and only the sphalerite without noticeable

mineral inclusions was prepared for EMPA and LA-ICP-MS analysis.

3.1. SEM and EMPA analysis

Quantitative analysis and element mapping of sphalerite were analyzed by JEOL JXA-8230 Electron Probe Micro Analyzer at the Key Laboratory of Mineralogy and Metallogeny, Guangzhou Institute of Geochemistry, Chinese Academy of Sciences. Quantitative analyses were carried out at an accelerating voltage of 20 kV, with a beam current of 20nA and a beam diameter of 1 μm. In this study, the following 7 elements were analyzed (with their detection limits in ppm): Fe (94.2), Zn (189), Cd (93.2), Cu (92.8), Mn (66.0), S (78.6), and Sn (140). Element mapping applied for sphalerite was conducted at an accelerating voltage of 20 kV, with a probe current of 100nA and a beam size of 1 μm. Elements chosen for element mapping include Fe, Cu, Zn, and Sn. Iron and Cu were analyzed by using a LIFH crystal. Zinc and Cu were analyzed by using LIF and PETJ crystals, respectively.

3.2. In-suit LA-ICP-MS trace element analysis

Trace element concentrations in sphalerite were measured by Laser Ablation Inductively-Coupled Plasma Mass Spectrometry on polished samples at the In-situ Mineral Geochemistry Lab, Ore deposit and Exploration Centre (ODEC), Hefei University of Technology, China. The analyses were carried out on an Agilent 7900 Quadrupole ICP-MS coupled to a Photon Machines Analyte HE 193-nm ArF Excimer Laser Ablation system equipped. Argon was used as the make-up gas and mixed with the carrier gas via a T-connector before entering the ICP (Ning et al., 2017; Wang et al., 2017). Each analysis was performed by a uniform spot size diameter of 40 μm at 7 Hz with energy of ~ 2 J/cm2 for 40 s after measuring the gas blank for 20 s. Standard reference materials NIST 610, NIST 612, and BCR-2G were used as external standards to plot calibration curve. Sulfide standard MASS-1 was used for unknown sample to evaluate the sulfide element accuracy during analysis.
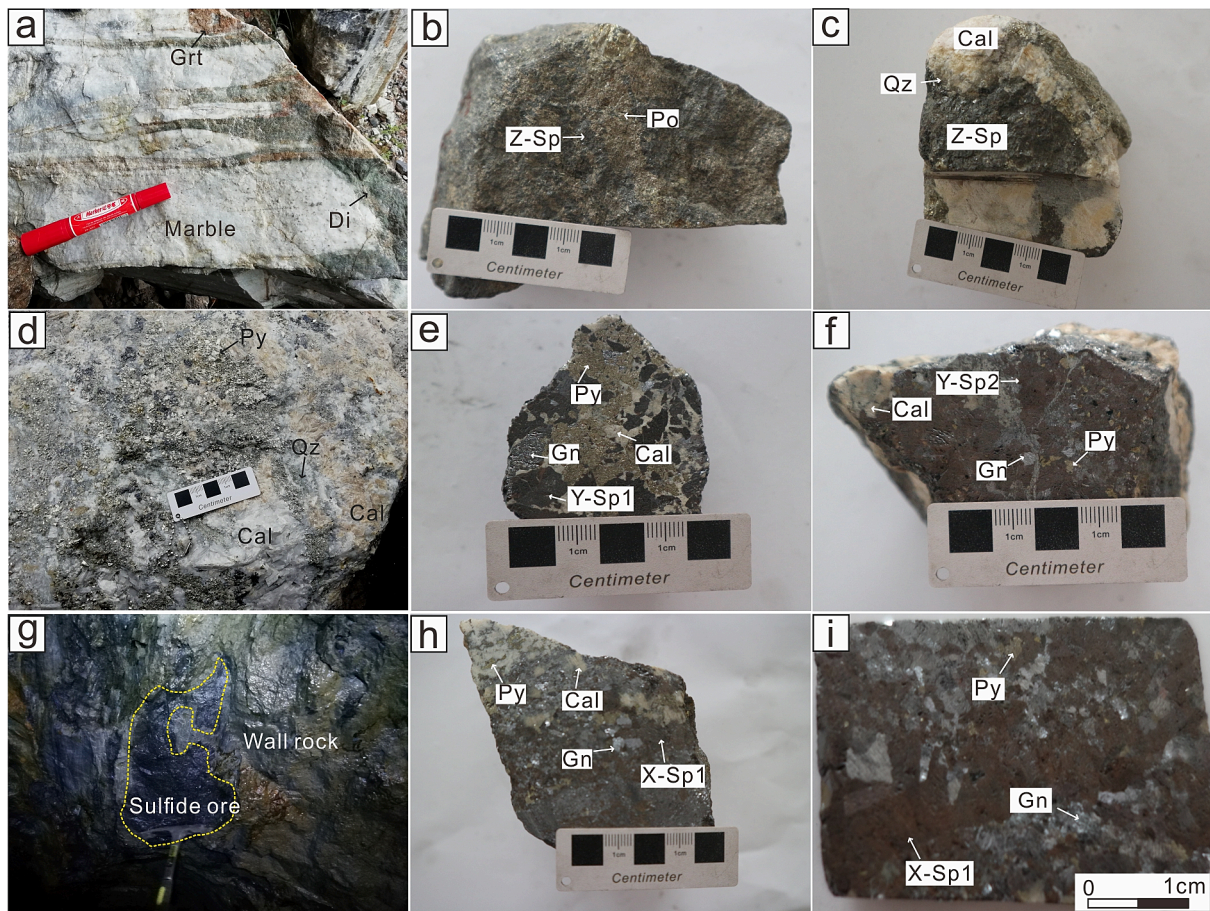
Fig. 3. Photographs showing the occurrences and textures of ores from the Zhongyuku (a-c), Yindonggou (d-f), and Xigou (g-i) ore blocks in the Chitudian deposit. (a) Skarnized marble. (b) Massive sulfide ore consists of banded sphalerite (Z-Sp) and pyrrhotite. (c) Late-stage calcite-quartz vein crosscut the sphalerite aggregate. (d) Early-stage calcite (yellow)-pyrite assemblage was replaced by late-stage calcite and quartz (white). (e) Sphalerite (Y-Sp1) is intergrown with galena, pyrite, and calcite. (f) Abundant sphalerites (Y-Sp2) coexist with galena, calcite, and minor pyrite. (g) Sulfide ore within wall rock. (h) X-Sp1 is intergrown with abundant galena, calcite, and minor pyrite. (i) Massive ore dominated by sphalerite (X-Sp1), galena, and minor pyrite. Abbreviations: Sp = sphalerite; Gn = Galena; Py = pyrite; Ccp = chalcopyrite; Po = pyrrhotite; Qz = quartz; Grt = garnet; Di = diopside; Cal = calcite.

The isotopes measured were ^{55}Mn, ^{57}Fe, ^{59}Co, ^{63}Cu, ^{66}Zn, ^{71}Ga, ^{72}Ge, ^{75}As, ^{77}Se, ^{107}Ag, ^{111}Cd, ^{115}In, ^{118}Sn, ^{121}Sb, and ^{208}Pb. Indium concentrations were corrected for the isobaric interference of ^{115}In and ^{115}Sn. The offline data processing was performed using a program called ICPMSDataCal (Liu et al., 2008). Trace element compositions of samples were calibrated against multiple-references materials with applying Zn values determined by EMPA as the internal normalization element.

Element maps were created by ablating sets of parallel line rasters in a grid across the sample. A beam size of 15 μm and scan speeds of 15 μm/s were chosen in this study. A laser repetition of 10 Hz was selected at a constant energy output of 50 mJ, resulting in an energy density of ~ 3 J/cm^2 at the target. A 20-s background acquisition was acquired at the start of scanning, and to allow for cell wash-out, gas stabilization, and computer processing, a delay of 20 s was used after ablation. Reference materials NIST 610 and GSE-1G at the start and end of each mapping were analyzed for data calibration. Images were compiled and processed using the program LIMS (Wang et al., 2017; Xiao et al., 2018). For each raster and every element, the average background was subtracted from its corresponding raster, and the rasters were compiled into a 2-D image displaying combined background/drift corrected intensity for each element (Xiao et al., 2018).

3.3. Principal component analysis (PCA)

Generally, the trace element dataset obtained by LA-ICP-MS contains multiple variables. The PCA, a multivariate statistical analysis method, can briefly reflect as much original information as possible by variables reduction, and the original data processed by PCA can be projected in two dimensions (Belissont et al., 2014; Frenzel et al., 2016; Bauer et al., 2019a). These two dimensions, corresponding to the most important two principal components, are directly determined as the first two eigenvectors of the correlation matrix with the highest eigenvalues. Consequently, the internal structure and variance of the original data can be extremely expressed by PCA. In this study, the dataset processed by PCA was log-transformed and filtered by the criteria suggested by Yuan et al. (2018). All the data were processed by the PCA module in OriginPro 9.0 software. More details about PCA can refer to Koch (2012) and Frenzel et al (2016).

4. Results

4.1. Petrographic observation

Sphalerite is the predominant ore mineral of the Zhongyuku (Z-Sp), Yindonggou (Y-Sp), and Xigou (X-Sp) ore blocks in the Chitudian deposit. Five types of sphalerite (Z-Sp, Y-Sp1, Y-Sp2, X-Sp1, and X-Sp2) are distinguished in this deposit, based on petrographic observations and sample locations.

In the ZOB, Z-Sp is abundant in the sulfide stage, showing black color and euhedral-subhedral crystals (Fig. 3b, c). It commonly coexists with
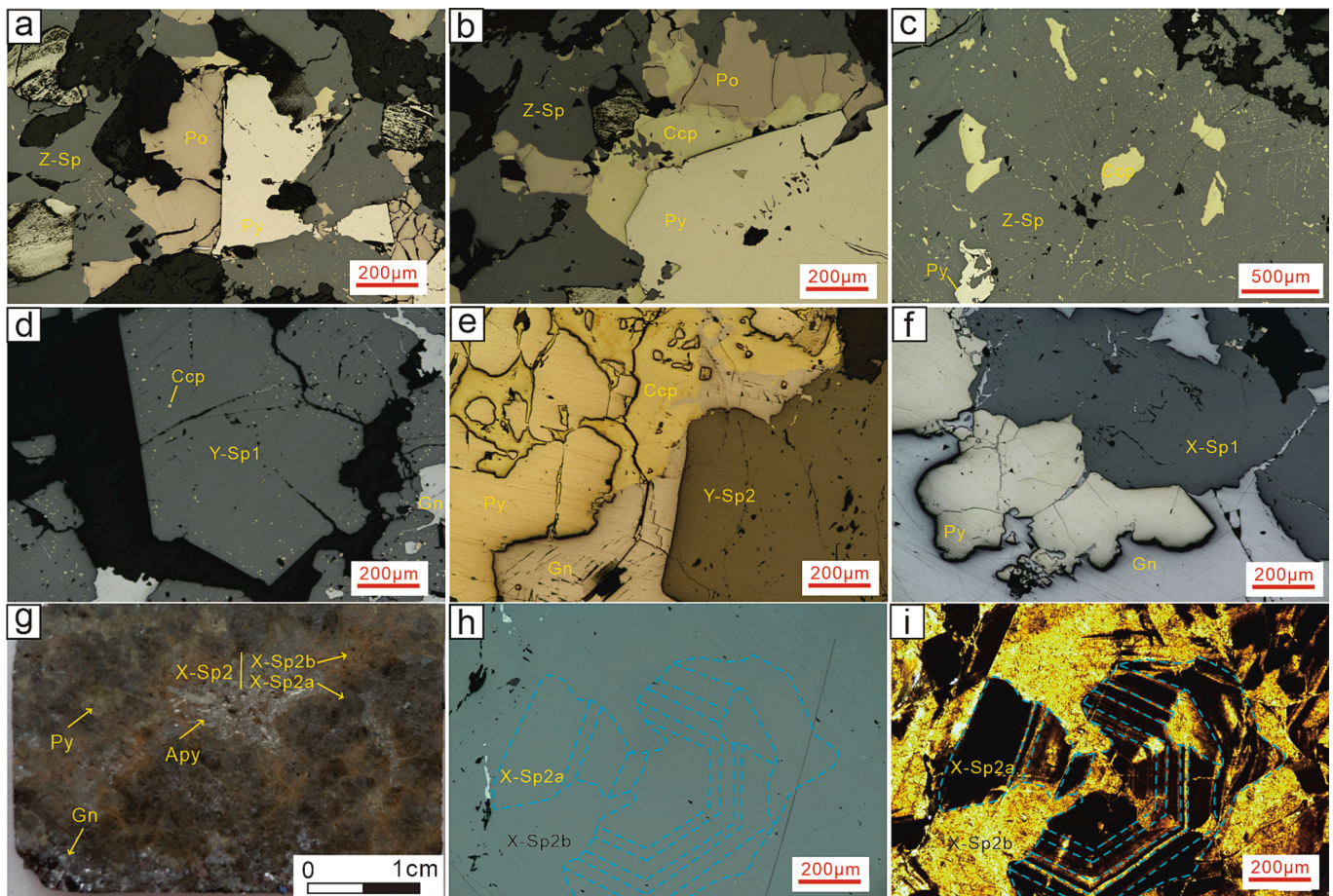
Fig. 4. Photomicrographs showing the representative ore mineral assemblages from the Zhongyuku (a-c), Yindonggou (d-f), and Xigou (g-i) ore blocks in the Chitudian deposit. (a) Z-Sp is co-crystalized with pyrite and pyrrhotite. (b) Anhedral Z-Sp coexists with chalcopyrite, pyrrhotite, and pyrite. (c) Granular pyrite was replaced by Z-Sp. (d) Euhedral Y-Sp1 containing abundant sulfide inclusions was replaced by gangue minerals. (e) Y-Sp2 is co-crystalized with galena and pyrite was replaced by chalcopyrite. (f) X-Sp1 and pyrite were replaced and crosscut by galena. (g) Polished sulfide sample containing sphalerite, galena, arsenopyrite, and pyrite. X-Sp2 consists of X-Sp2a (black) and X-Sp2b (brown), and X-Sp2a is enclosed by X-Sp2b. (h) Reflected light photomicrographs of X-Sp2. The contours of the X-Sp2a were shown by the dotted line. (i) Transmitted light photomicrographs of X-Sp2 corresponding to (h). Abbreviations: Sp = sphalerite; Gn = Galena; Py = pyrite; Apy = arsenopyrite; Ccp = chalcopyrite; Po = pyrrhotite; Qz = quartz; Cal = calcite.

pyrrhotite, pyrite, and chalcopyrite which occurs as separate grains or inclusions in sphalerite (Fig. 4a-c).

Y-Sp1 and Y-Sp2 are identified in the YOB with different appearances. Y-Sp1 is mainly associated with coarse-grained calcite, galena, and pyrite with black color and euhedral crystals (Fig. 3e and 4d). It is also characterized by abundant inclusions of chalcopyrite (Fig. 4d). In contrast with Y-Sp1, Y-Sp2 shows a brown color in hand specimens and contains a few sulfide inclusions (Fig. 3f and 4e). This type is closely intergrown with quartz, calcite, pyrite, galena, and chalcopyrite (Fig. 4e).

X-Sp1 and X-Sp2 were sampled from the 980 m and 900 m levels of the S130 ore vein, respectively (Fig. 5a). Both of them are associated with abundant galena and minor pyrite (Fig. 3g, h, and 4 g). X-Sp1 is dark brown (Fig. 3g, h), and the boundary between X-Sp1 and coexisted minerals is clear in hand specimens and photomicrographs (Fig. 3g, h, and 4f). In contrast to X-Sp1, X-Sp2 has a complex texture in hand specimens, in which dark sphalerite (X-Sp2a) is surrounded by brown sphalerite (X-Sp2b) (Fig. 4g). However, these two subtypes of sphalerite cannot be distinguished under reflected light (Fig. 4h) but are well presented under transmitted light in photomicrographs (Fig. 4i). The backscattered electron (BSE) images show that the fractured and zoned X-Sp2a was dissolved and replaced by X-Sp2b (Fig. 5f-k). Some stannite inclusions were observed along the margin and microfractures of X-Sp2a (Fig. 5h-k). Moreover, the sulfides from the same sample as X-Sp2

(including X-Sp2a and X-Sp2b) also have abundant microfractures that are filled with X-Sp2b (Fig. 5b-c), and the zoning structures are revealed by BSE images (Fig. 5d-e).

4.2. Major and trace elements in sphalerite

A total of 118 spots were analyzed by EMPA and LA-ICP-MS, respectively. The contents of major and trace elements are summarized in Table 1 and detailed analytical data are given in Electronic Supplementary Materials (ESM), among which some elements with higher content are presented in Fig. 6 and discussed below. Trace elements in sphalerite from skarn ores (Z-Sp) vary in a limited range compared with sphalerite from hydrothermal-vein ores (Y-Sp1, Y-Sp2, X-Sp1, X-Sp2a, and X-Sp2b). Generally, the composition of sphalerite varies systematically from skarn ores to hydrothermal-vein ores.

The concentration of Fe in sphalerite decreases, whereas the concentration of Zn increases gradually from Z-Sp to X-Sp2b (Fig. 6a, b). The concentration of Fe in sphalerite is closely related to the color of the studied sphalerite crystals. The brown sphalerite (X-Sp2b) found in XOB has the lowest Fe concentration (av. (average) = 4.19 wt%). However, the black sphalerite found in ZOB has the highest Fe concentration (Z-Sp; av. = 10.56 wt%). Although the concentration of Mn shows a similar distribution trend as Fe, a slight increase was observed in X-Sp2a and X-Sp2b (Fig. 6c). Both Fe and Mn tend to concentrate in sphalerite from
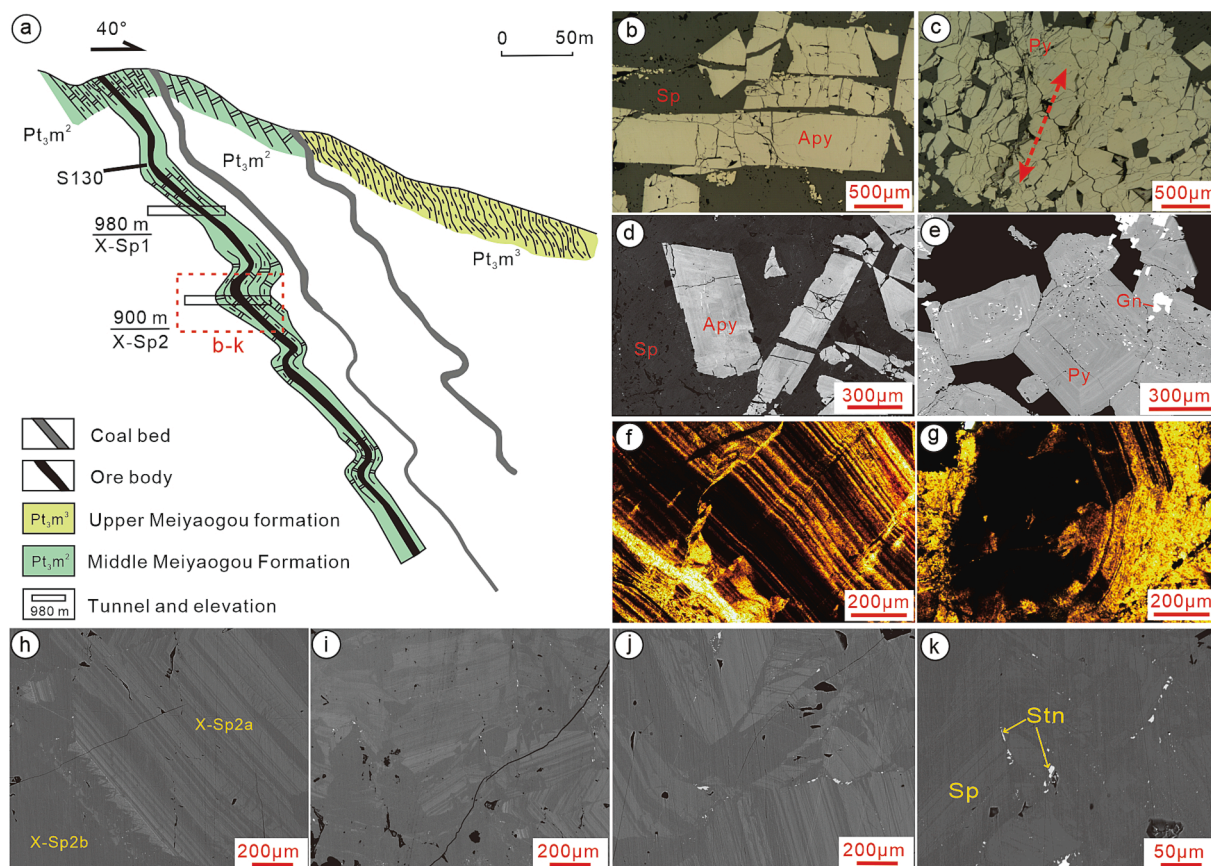
Fig. 5. Textures of sulfide from the core of folded S130 vein. (a) Cross-section through the folded S130 vein of the Xigou ore block, Chitudian deposit. (b-c) Textures of arsenopyrite and pyrite under reflected light. (d-e) BSE image showing the zoning structure in arsenopyrite and pyrite. (f-g) Textures of X-Sp2 under transmitted light. (h-k) BSE image showing the textures of X-Sp2 (including X-Sp2a and X-Sp2b). Stannite inclusions were observed in microfractures of X-Sp2a. Abbreviations: Sp = sphalerite; Py = pyrite; Apy = arsenopyrite; Stn = stannite.

Table 1
Summary of element contents in sphalerite from the Chitudian deposit. Zinc and Fe are given in wt% (EPMA) and all other trace elements in ppm (LA-ICP-MS).

Type		Zn	Fe	Mn	Cd	Cu	In	Ga	Ge	Ag	Sn
Z-Sp	Min	53.7	9.14	2987	1441	60.6	103	0.53	0.28	0.49	0.06
(n = 29)	Max	56.7	11.3	8969	1997	197	322	9.18	0.78	3.22	0.51
	Average	54.8	10.6	5380	1660	104	155	3.30	0.46	1.08	0.15
Y-Sp1	Min	54.3	7.13	292	2861	49.2	31.9	6.96	0.30	3.69	2.15
(n = 19)	Max	59.3	11.5	3167	5145	4564	2114	52.4	2.07	154	132
	Average	56.2	9.71	1325	3902	752	561	21.0	0.62	50.7	39.0
Y-Sp2	Min	57.5	3.19	185	1727	79.5	2.63	15.3	0.31	5.76	44.5
(n = 17)	Max	64.4	7.93	764	3114	1026	47.4	37.3	0.95	101	949
	Average	60.6	5.75	387	2410	286	12.8	29.2	0.52	26.4	206
X-Sp1	Min	58.7	5.30	255	2395	16.6	0.75	5.77	0.29	2.27	0.66
(n = 19)	Max	60.7	7.03	421	4567	714	80.2	18.0	0.67	17.0	669
	Average	59.8	5.99	311	3177	201	15.4	12.3	0.42	8.32	169
X-Sp2a	Min	58.8	3.83	381	2271	716	3.41	85.2	0.52	5.36	396
(n = 17)	Max	62.7	5.55	834	4021	10,045	211	333	3.18	45.7	9893
	Average	61.7	4.29	589	2962	3733	29.6	179	1.79	24.8	3469
X-Sp2b	Min	61.4	3.84	400	2284	43.4	16.4	33.7	0.32	2.62	3.57
(n = 17)	Max	63.1	5.44	769	3869	755	422	528	0.46	16.6	89.7
	Average	62.3	4.17	548	2818	196	136	123	0.39	6.96	16.8

skarn ores rather than hydrothermal ores. In contrast to Mn and Fe, Cd and Ag are primarily concentrated in sphalerite from hydrothermal ores, in which sphalerites have an average concentration of 23.7 ppm for Ag and 3075 ppm for Cd (Fig. 6d, e). However, the average concentrations of Ag and Cd for Z-Sp are as low as 1.08 ppm and 1660 ppm, respectively.

In terms of Ga, the lowest value occurs in Z-Sp (av. = 3.30 ppm), and the highest value occurs in X-Sp2a (av. = 179 ppm). Overall, the concentration of Ga shows an increasing trend from skarn ores to hydrothermal-vein ores (Fig. 6f). In Fig. 6g and h, Cu and Sn are found in abundant amounts in sphalerite from hydrothermal-vein ores (Table 1), particularly in X-Sp2a (av. = 3733 ppm for Cu and 3469 ppm for Sn). In contrast, the concentrations of Cu and Sn are relatively poor in skarn ores, in which their average values are 104 ppm for Cu and 0.15 ppm for Sn. Although the concentrations of Cu and Sn significantly vary in different types of sphalerite, their distribution trends are similar (Fig. 6g,
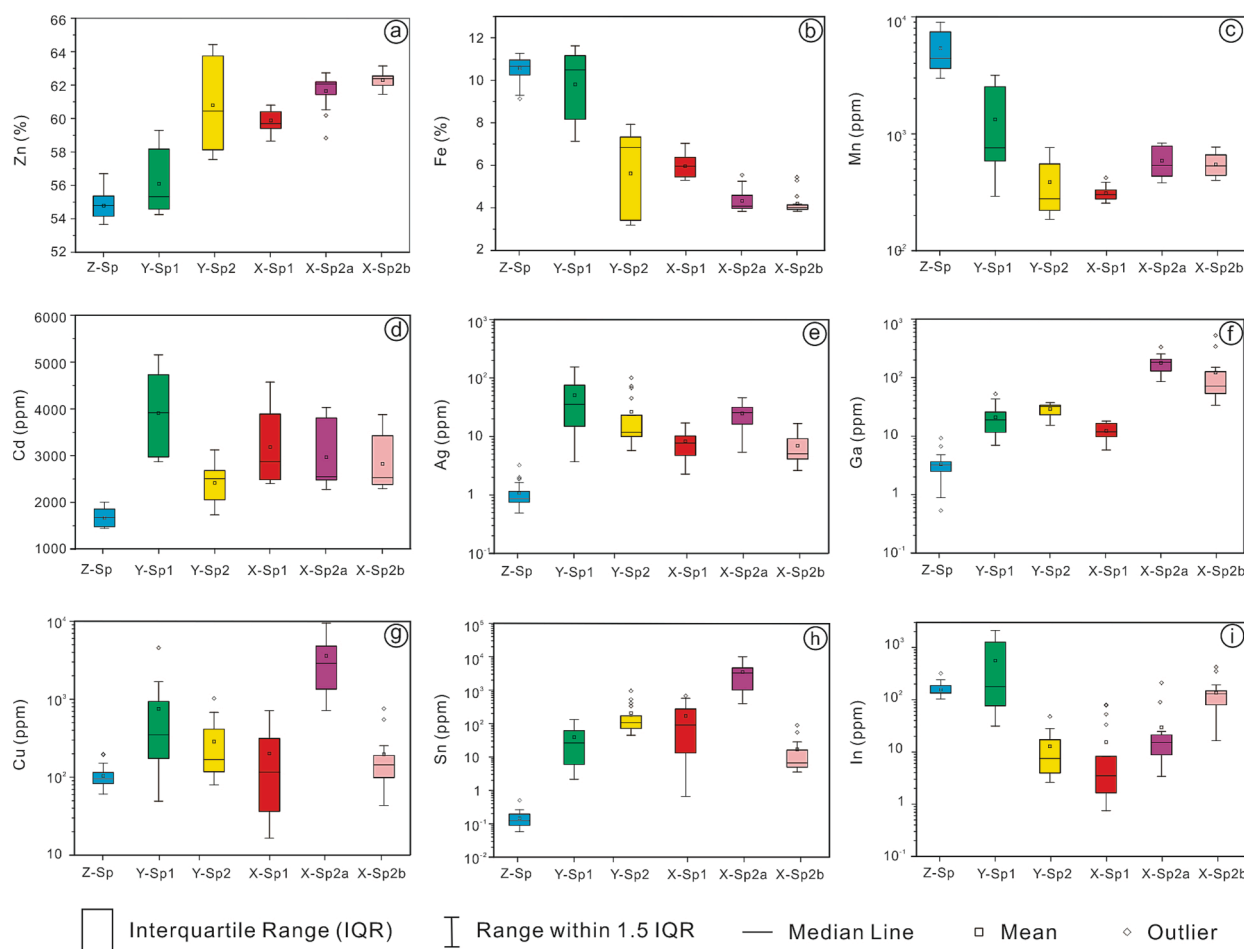
Fig. 6. Box-whisker plots of the major and trace element compositions of sphalerite from the Chitudian deposit. The box for each element represents the 25% (lower margin) to 75% (upper margin) data ranges. The square and diamond symbols represent the mean and outlier, respectively. The median value is shown as horizontal line in each box.

h). Different from other elements, the distribution trend of In is "U-shaped" (Fig. 6i). The most In-rich sphalerite is Y-Sp1 (av. = 561 ppm), followed by Z-Sp (av. = 155 ppm) and X-Sp2b (av. = 136 ppm). It is noteworthy that X-Sp2a is closely related to X-Sp2b in spatial (Fig. 5f-k), but the concentrations of Cu, Sn, and In are much different between them. X-Sp2a is generally characterized by higher Cu (av. = 3733 ppm), Sn (av. = 3469 ppm), and lower In (av. = 29.6 ppm), relative to X-Sp2b (av. = 196 ppm for Cu, 16.8 ppm for Sn, 136 ppm for In). Furthermore, the trace element variations between X-Sp2a and X-Sp2b are presented by element mapping results.

4.3. Element mapping

Distinct changes in the concentrations of Cu, Sn, and In may indicate a special mechanism that controls the element distribution pattern between X-Sp2a and X-Sp2b. Thus, element mapping was conducted on X-Sp2 (Figs. 7 and 8). According to LA-ICP-MS element maps, Fe and Cd show relatively homogenous distributions (Fig. 7c, d). Gallium and Ag display erratic distributions between X-Sp2a and X-Sp2b, and weak zonation can be observed (Fig. 7e, f). Importantly, it seems that In prefers to concentrate in X-Sp2b (light part) rather than X-Sp2a (dark part) (Fig. 7g). In contrast to In, Sn, and Cu are spatially coupled in X-Sp2a (Fig. 7h, i). Furthermore, the EMPA element maps with higher resolution show that Sn and Cu are significantly enriched in the rhythmic bands of X-Sp2a (Fig. 8). Abundant stannite microinclusions (<10 μm) are distributed along the microfractures of X-Sp2a.

4.4. Principal component analysis of in situ datasets

The results of the PCA applied to the sphalerite trace element dataset are shown in Fig. 9, where the first two principles capture about 70 % of element content variability (Fig. 9c). Principal Component 1 (PC1) is a measure of Sn, Ga, Ag, and Cd contents of all the sphalerite subtypes (Fig. 9a, d). Principal Component 2 (PC2) is a measure of Fe, Mn, Cu, Ge, and In contents (Fig. 9a, d). In detail, PC2 can be further divided into subgroups: PC2-1 (Fe, Mn, and In) and PC2-2 (Ge and Cu) (Fig. 9a and d). All of them are positively related and have positive signs (Fig. 9d). When all spots are projected on the PC1 vs. PC2 plane (Fig. 9b), sphalerite samples can be classified into two groups: Fe-rich sphalerites and Fe-poor sphalerites, where the former is composed of Z-Sp and Y-Sp1 and the latter is composed of Y-Sp2, X-Sp1, X-Sp2a, and X-Sp2b. Although all of the Fe-poor sphalerites are taken from hydrothermal-vein ores, X-Sp2a is independent of the others.

PCA was further applied to X-Sp2a and X-Sp2b to investigate whether they were different in element correlation clusters (Fig. 10). The results highlight the variable behaviors of In and Ga in these two sphalerite subtypes. For X-Sp2a, Sn, Cu, and Ag are clustered, while Ga and In are independent of other elements (Fig. 10A). In contrast, In-Ga-Sn-Gu are clustered in X-Sp2b (Fig. 10B).
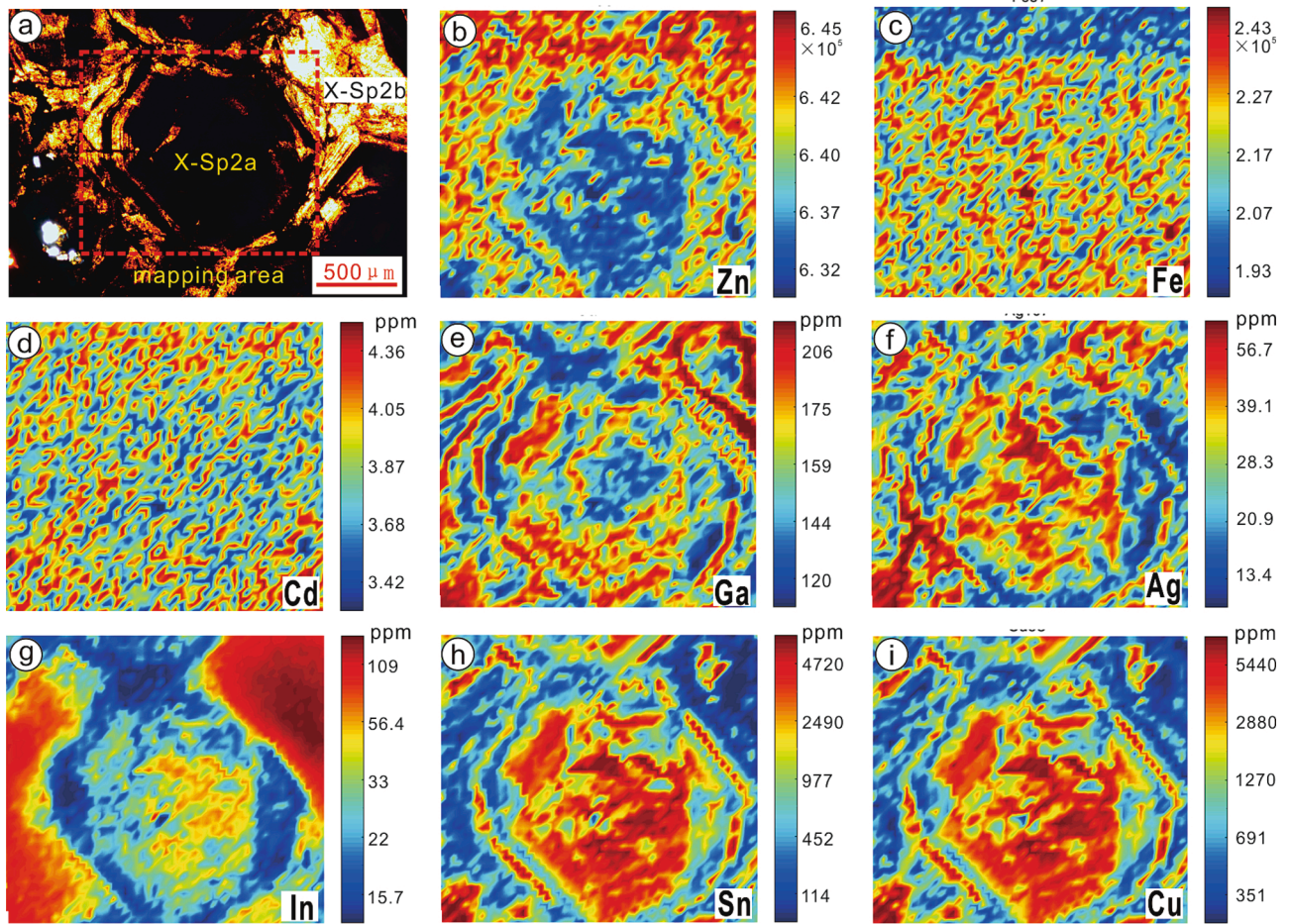
Fig. 7. LA-ICP-MS element maps of X-Sp2. (a) Photomicrograph of mapped sphalerite (X-Sp2) under transmitted light. (b–i) Element maps for Zn, Fe, Cd, Ag, Ga, In, Sn, and Cu respectively.

5. Discussion

5.1. Correlation trend and element substitution in sphalerite

Element substitution within sphalerite has been extensively investigated in previous studies because it is of great significance to reveal the mineralization process and ore genesis (Cook et al., 2009, 2012; Belissont et al., 2014; Frenzel et al., 2016, 2020; Wei et al., 2021). However, the concentrations of trace elements in sphalerite are the results of lattice-bound solid solutions or mineral inclusions (Cook et al., 2009; George et al., 2016). Thus, it is necessary to first clarify the occurrence of trace elements in sphalerite.

Time-resolved depth profiles are usually used to judge the occurrence of trace elements in minerals (Cook et al., 2009; Belissont et al., 2014). When a mineral contains microscopic inclusions, profiles exhibit ragged or spiky patterns. In contrast, flat profiles suggest that the elements are probably present as solid solutions. Most analysis spots yield smooth element signals in our dataset, suggesting compositional homogeneity within sphalerite grains and the occurrence of element as a solid solution (Fig. 11). However, some samples display ragged Cu, Pb, and Sn signals, indicating the existence of Cu-, Pb-, and Sn-bearing mineral inclusions in sphalerite (Yuan et al., 2018; Zhuang et al., 2019) (Fig. 11b, d, f). These results have a good agreement with the petrographic observations (Figs. 4 and 5).

Iron, Mn, and Cd are the most abundant trace elements in sphalerite from the Chitudian deposit (Fig. 6). Previous studies suggested that divalent cations, such as Fe^{2+}, Mn^{2+}, and Cd^{2+}, are incorporated into sphalerite by substituting for Zn^{2+} directly because they have similar ion

radii and oxidation states in tetrahedral coordination (Ye et al., 2011; Wei et al., 2018; Xing et al., 2021). In this study, Zn is negatively correlated with Fe, Mn, and Cd, suggesting a simple substitution: $Zn^{2+} \leftrightarrow$ (Fe, Mn, Cd) $^{2+}$ (Fig. 12a).

In addition, several more complicated substitution mechanisms that lead to the enrichment of mono-, tri-, and tetravalent cations (i.e., Ag^+, Cu^+, Ga^{3+}, In^{3+}, Ge^{4+}, and Sn^{4+}) were also proposed (Cook et al., 2009; Ye et al., 2011; Frenzel et al., 2016). For example, trivalent cations, such as In^{3+} and Ga^{3+}, can be incorporated into sphalerite by a couple substitution: $(In, Ga)^{3+} + (Cu, Ag)^+ \leftrightarrow 2Zn^{2+}$ (Murakami and Ishihara, 2013), of which Cu^+ and Ag^+ are needed to balance charge in sphalerite structure. In this study, the concentration of Ag was significantly lower than that of Cu, making Cu the predominant monovalent cation (Fig. 6). Consequently, Cu is supposed to be positively correlated with the trivalent cations. As shown in Fig. 12b, a positive correlation between Cu and In was exhibited by Fe-rich sphalerite types (Z-Sp and Y-Sp1), indicating the couple substitution of $In^{3+} + Cu^+ \leftrightarrow 2Zn^{2+}$ (Xu et al., 2021b). But the Cu-In correlation is obscure in Fe-poor sphalerite types (Y-Sp2, X-Sp1, X-Sp2a, and X-Sp2b) (Fig. 12b), where a strong positive correlation between Sn and Cu, with a ratio of (Cu:Sn) $_{mol}$ = 2, raises the substitution of $2Cu^+ + Sn^{4+} \leftrightarrow 3Zn^{2+}$ (Fig. 12c) (Murakami and Ishihara, 2013). However, it should be emphasized that because stannite was found in X-Sp2 (Fig. 5h-k), we cannot exclude the effect of stannite (Cu_2FeSnS_4) on the atom ratio of Cu:Sn. The substitution of Sn within sphalerite requires further verification by using techniques (e.g., XANES and HRTEM) that are appropriate for accurate assessment of the oxidation state and occurrence of Sn.

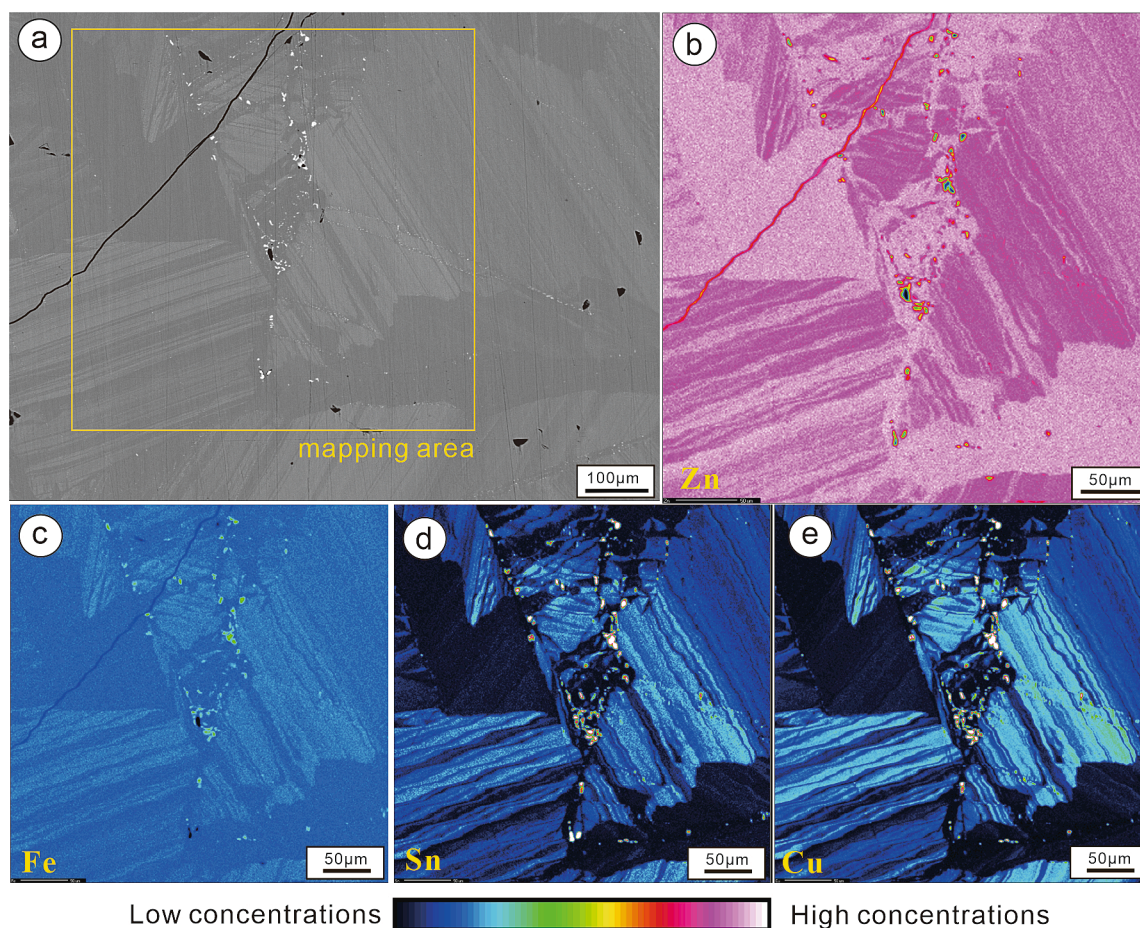Previous works have suggested that In and Sn may be incorporated

Fig. 8. EMPA element maps of X-Sp2. (a) BSE image of X-Sp2. (b-e) Elemental maps for Zn, Fe, Sn, and Cu respectively.

into sphalerite by couple substitutions as $In^{3+} + Sn^{3+} + \square$ (vacancy) $\leftrightarrow$ $3Zn^{2+}$ or $In^{3+} + Sn^{2+} + Ag^+ /Cu^+ \leftrightarrow 3Zn^{2+}$ (Belissont et al., 2014; Frenzel et al., 2016; Wei et al., 2018; Oyebamiji et al., 2020; Xu et al., 2021a), but no evident correlation was observed between In and Sn in our dataset (Fig. 12d). A weak correlation between Ga and Cu could result from the low concentration of Ga in most sphalerite samples (Table 1) (Fig. 12e). However, the positive Ga-Cu correlation was observed in X-Sp2b, indicating the incorporation of Ga into X-Sp2b via a couple substitution of $Ga^{3+} + Cu^+ \leftrightarrow 2Zn^{2+}$ (Fig. 12e) (Frenzel et al., 2016).

Overall, the correlation between mono-, tri-, and tetravalent cations is further demonstrated by Fig. 12f. The concentrations of monovalent cations (Cu and Ag) are close to the sum of tri- and tetravalent cations (Ga, In, and Sn). Consequently, Cu (and Ag to a lesser extent) could be responsible for the incorporation of these trivalent/tetravalent cations. Several data that plot above the positive correlation trend could be attributed to abundant chalcopyrite inclusions in Y-Sp1 (Fig. 4d, Fig. 11b, and Fig. 12f).

5.2. Distribution of Cd, Ga, and In in the Chitudian deposit

It is generally accepted that Ga, Ge, and Cd have a preference for low-temperature deposits, while In is dominantly concentrated in granite-related deposits with higher mineralization temperatures (Zhang, 1987; Tu, 2004; Cook et al., 2009; Wen et al., 2019; Zhou and Wen, 2021). The Pb-Zn-Ag deposits in the Luanchuan ore district are considered to be genetically associated with the Mesozoic granite, and the mineralization temperatures of main stage range from 200 °C to 350 °C (Duan et al., 2011; Cao et al., 2015; Xu, 2015). In this study, the Zn/Cd ratios of the sphalerite from the Chitudian deposit are almost always

below 300, with an average value of 182, which is consistent with the Zn/Cd ratio of magmatic-hydrothermal sphalerite (<300) (Wen et al., 2016). Therefore, it can be expected that the Chitudian deposit contains higher In and relatively lower Ga, Ge, and Cd.

The LA-ICP-MS results show that the concentration of Ge (<4 ppm) is indeed low in sphalerite from the Chitudian deposit. As for Cd, it is the most important trace element in sphalerite, except for Fe and Mn, and it ranges from 1411 to 5145 ppm (Table 1). The average concentration of Cd is 2728 ppm, which is similar to high-temperature Pb-Zn deposits (~2000 ppm), but distinct from low-temperature Pb-Zn deposits (~6000 ppm) (Schwartz, 2000). In detail, Cd is mainly concentrated in the sphalerites from hydrothermal-vein ores (3075 ppm) rather than skarn ores (1660 ppm), indicating that the former contains more Cd metal than the latter. The spot analysis results also suggest that Cd is homogeneously distributed in the sphalerite grains, regardless of sphalerite types, because the concentration of Cd varies in a limited range for each sample (ESM: Table S1 and S2).

In terms of Ga, 84 spots give an average value of 14.6 ppm. The enrichment of Ga was only noticed in X-Sp2a (179 ppm) and X-Sp2b (123 ppm) (Fig. 6f). Since the sphalerite formed in magmatic-hydrothermal systems is generally considered to be Ga-poor (<10 ppm), a Ga-bearing source is needed to explain the enrichment of Ga in X-Sp2 (including X-Sp2a and X-Sp2b). In the Luanchuan ore district, the Meiyaogou Formation is an important ore-bearing stratum with numerous Pb-Zn-Ag veins, and this sedimentary unit contains several coal beds with a total thickness of > 150 m (Figs. 2 and 5). Chen et al. (1989) found that the Ga concentrations of the coal beds in the Luanchuan ore district are higher than the minimum grade for industrial operation (30 ppm), and Ga can be extracted as byproduct from the coal beds. Moreover, Zuo (2016) systemically investigated the chemical
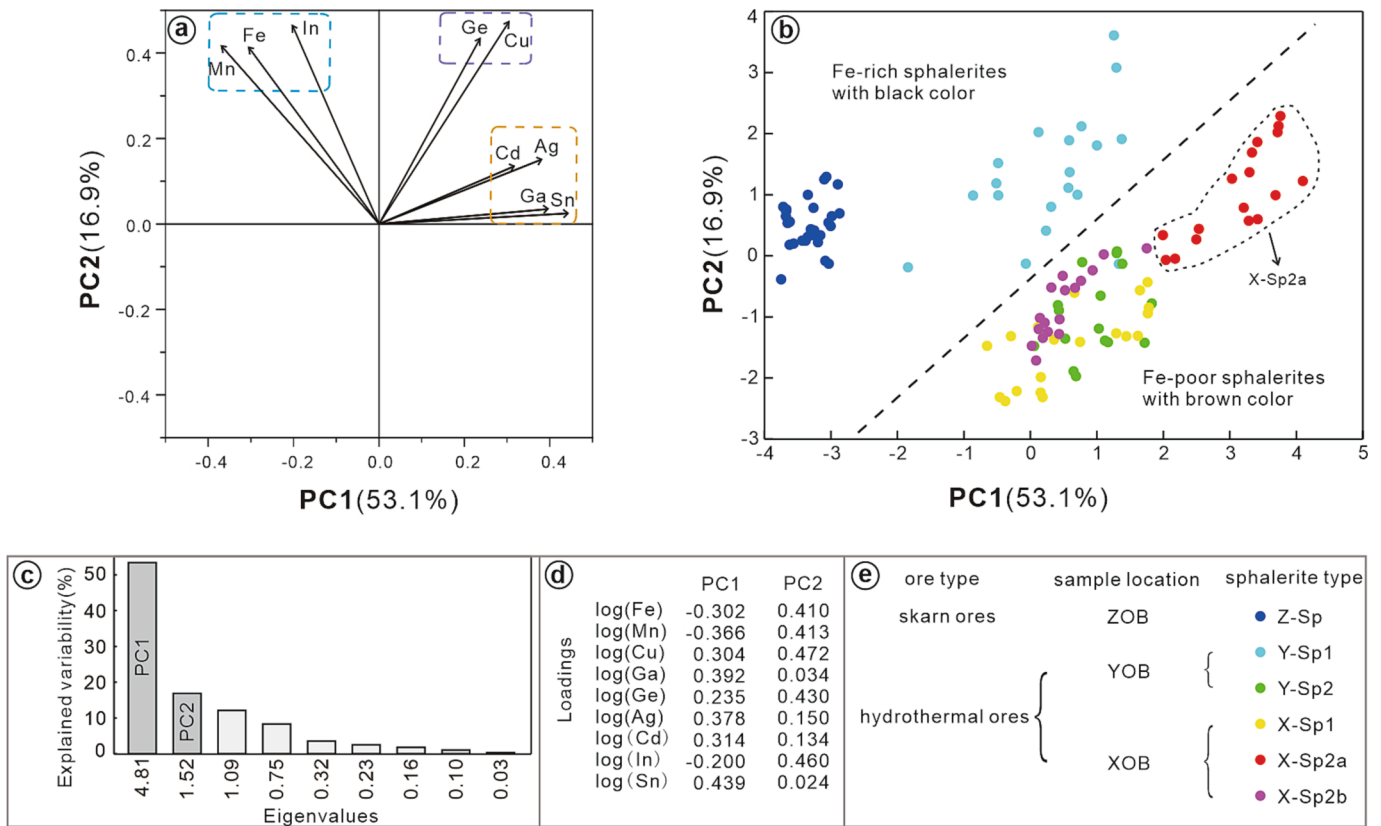
Fig. 9. Principal component analysis of the trace element contents (log-transformed) in sphalerite. (a) Elements plotted on the PC1 vs. PC2 plane (explaining 70.0 % of element content variability). The framed groups of elements with similar behavior. (b) Spot analyses plotted on the PC1 vs. PC2 plane. (c) Eigenvalues of the principal components. (d) Loadings of the principal components. (e) Data legend and sample information. Note that the angles of the arrows in (a) correspond to the element correlations. If the angle between two arrows is either close to 0° or 180°, they are positively or negatively correlated. If the angle between two arrows is close to 90°, then they are uncorrelated.
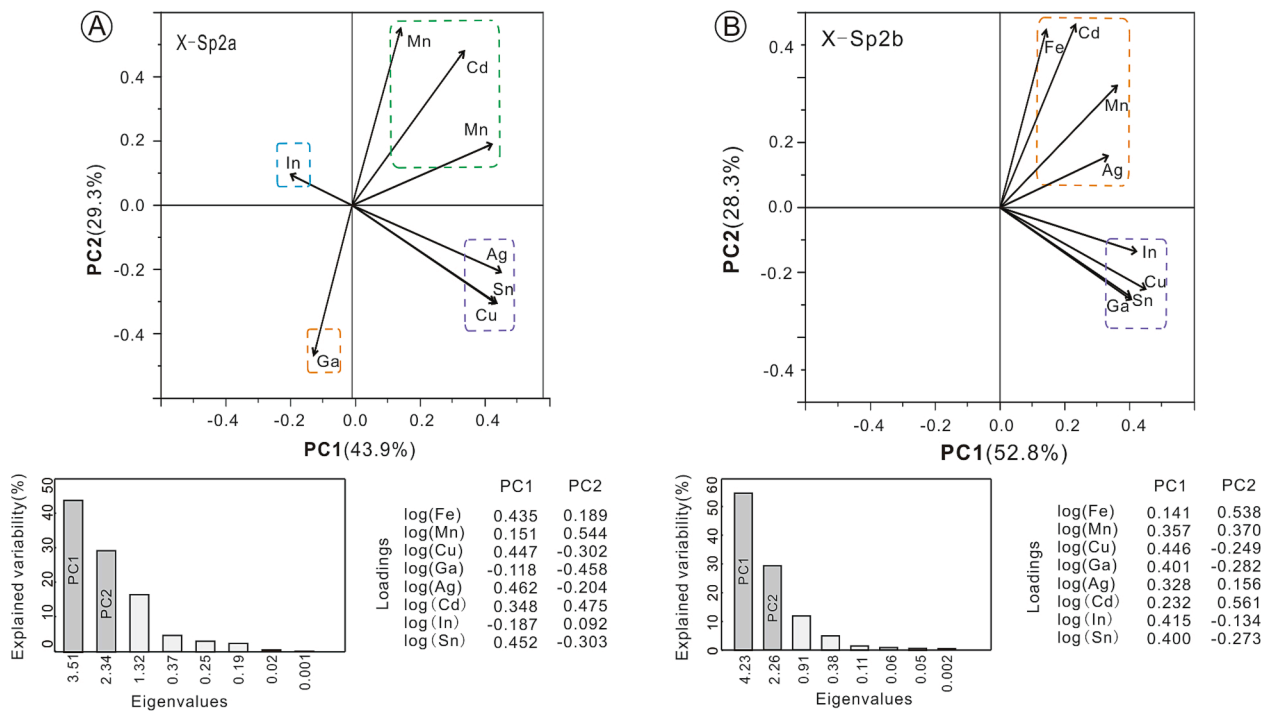

Fig. 10. Principal component analysis of the trace element contents (log-transformed) in X-Sp2a (A) and X-Sp2b (B). Upper part of (A): Elements plotted on the PC1 vs. PC2 plane (explaining 73.2 % of element content variability). Lower part of (A): eigenvalues and loadings of the principal components. Upper part of (B): Elements plotted on the PC1 vs. PC2 plane (explaining 81.1 % of element content variability). Lower part of B: eigenvalues and loadings of the principal components.
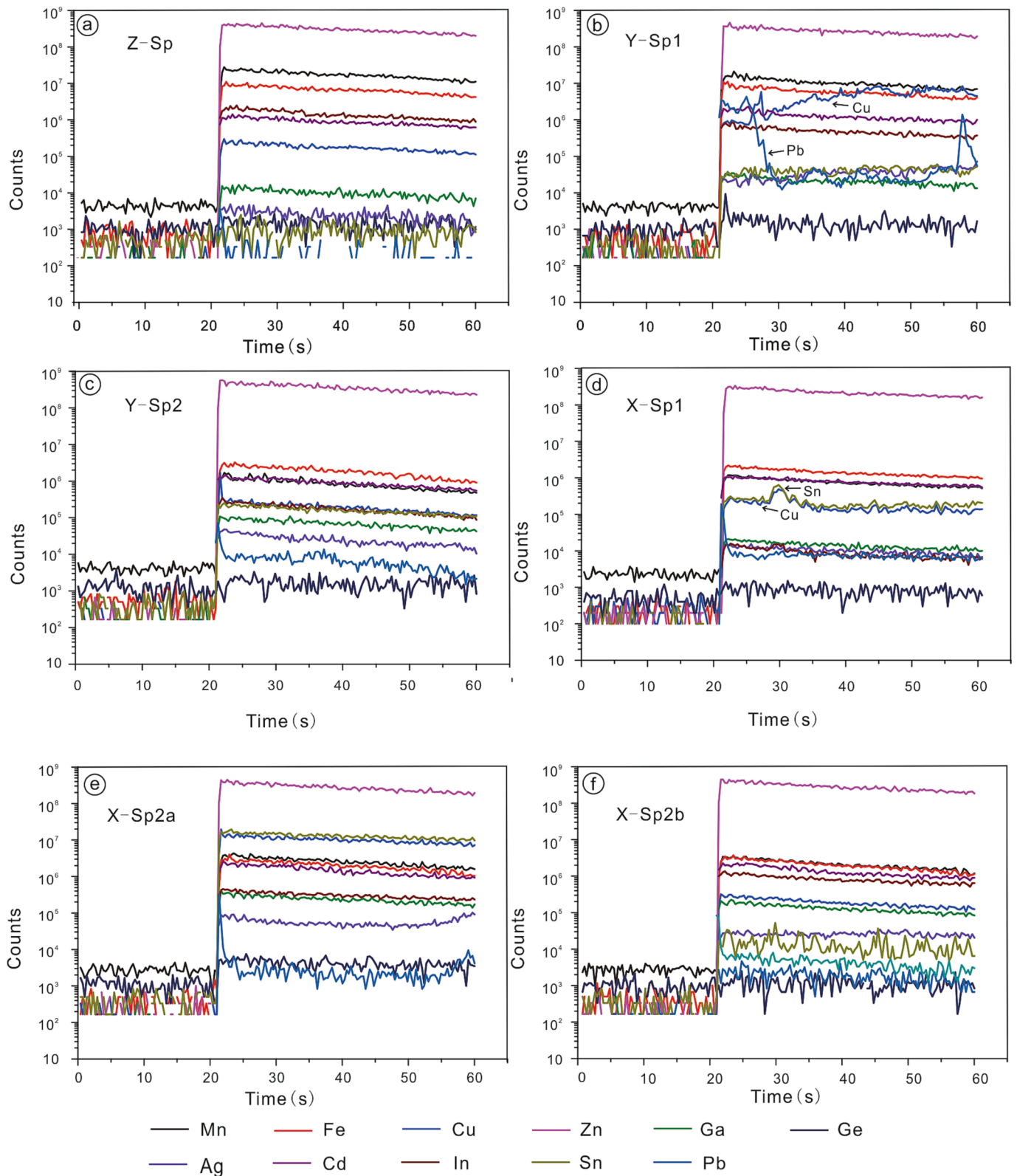
Fig. 11. Representative time-resolved depth profiles for selected elements in sphalerite. Smooth signals for Ga, Cd, and In indicate that such critical metals are relatively homogeneous in the sphalerite analyzed in this study.

composition of the black shales in the SNCC, and found that the highest Ga concentration (31.18 ppm) occurred in the coal samples from the Meiyaogou Formation. Considering that X-Sp2 is sampled from the strong deformed location of the folded S130 vein (Fig. 5a), the abrupt increases of Ga could be attributed to the Ga-bearing coal beds of the

Meiyaogou Formation. When the coal beds and S130 vein suffered from folding, abundant cleavages developed at the strongly deformed locations (such as the core of the fold), which provided permeable channels for hydrothermal fluid flow (Lee et al., 2019). As a result, Ga was leached from the coal beds by extensive water–rock interactions and
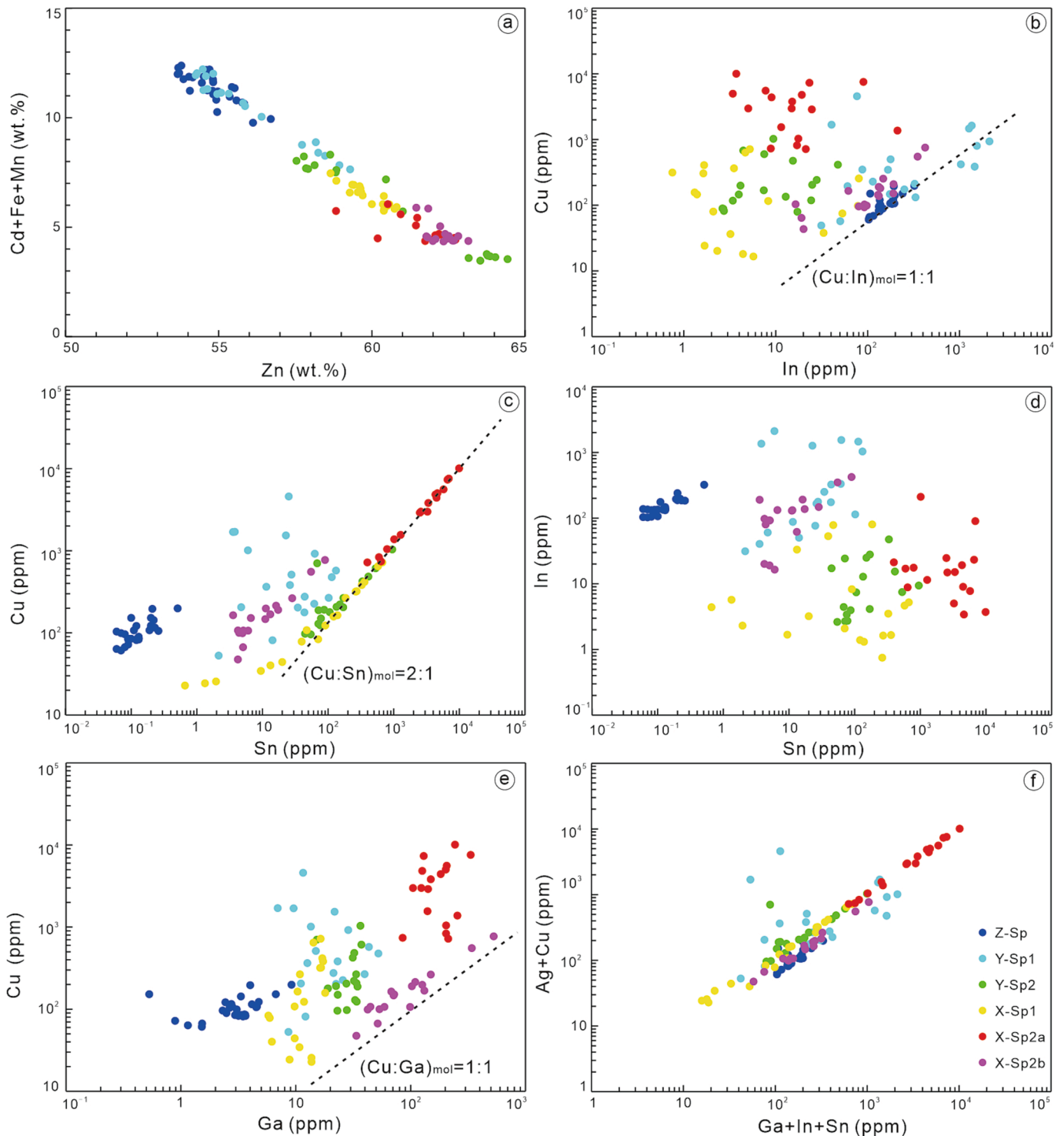
Fig. 12. Correlation plots of the major and trace element in sphalerite: (a) (Cd + Fe + Mn) vs. Zn; (b) Cu vs. In; (c) Cu vs. Sn; (d) In vs. Sn; (e) Cu vs. Ga; (f) (Ag + Cu) vs. (Ga + In + Sn).

subsequently sequestered by X-Sp2. This hypothesis is further supported by previous isotope (C-H-O-S-Pb-Sr) data (Cao et al., 2015), which define an increasing contribution of wall rock-derived materials to the distal Pb–Zn–Ag mineralization in the Luanchuan ore district.

Indium is a temperature-dependent element, and the concentrations of Fe, Mn, In, Ga, and Ge in sphalerite were applied to estimate the formation temperature of Zn-bearing ores (Frenzel et al., 2016). For instance, the higher concentrations of In and Fe in sphalerite generally imply higher formation temperatures. Previous microthermometry data

of fluid inclusions show that the mineralization temperature successively decreases from the ZOB, YOB, to XOB (Duan et al., 2011; Cao et al., 2015), corresponding to the increasing distance to magmatic intrusion (Fig. 2b). This understanding is reinforced by the decreasing contents of Fe from Z-Sp to X-Sp2b (Fig. 6b). Thus, In is expected to maintain a similar decreasing trend as Fe, but a slight increase in In was observed in X-Sp2a (av. = 29.6 ppm), and a distinct increase in In was observed in X-Sp2b (av. = 136 ppm) (Fig. 6i). When it comes to element correlation, In and Ga are expected to be positively correlated with Cu

(as discussed in section 5.1). The PCA results show that the In-Cu and In-Ga correlations are absent in X-Sp2a but occur in X-Sp2b (Fig. 10). These results may indicate an unknown mechanism that controls the abnormal element concentration and correlation in X-Sp2, as further discussed below.

5.3. Trace element remobilization induced by tectonic deformation

Sphalerite is widespread in the Chitudian deposit, but only the sphalerites (X-Sp2) from the deformed location (900 m level) of S130 vein have a complex texture (Fig. 5). In photomicrographs, the fragments of X-Sp2a were cemented or cut through by X-Sp2b (Fig. 4i and 5f-k), and obvious dislocation was observed in the rhythm bands of X-Sp2a (Fig. 5f). The pyrite and arsenopyrite from the 900 m level of S130 vein also have abundant microfractures with a preferred orientation (Fig. 5b, c), and these micro-fractures are generally filled with X-Sp2b. All of these textural evidences suggest that the sulfide in the deformed location of S130 vein has experienced brittle-plastic deformation (Fig. 5). Actually, the Vickers hardness of sphalerite (128–276 kg·mm^{-2}) is significantly lower than that of others, such as arsenopyrite (715–1354 kg·mm^{-2}), pyrrhotite (230–390 kg·mm^{-2}), and pyrite (913–2056 kg·mm^{-2}), resulting in a poor ability to resist tectonic modification (Shang et al., 2007). Various experimental deformation studies have confirmed that sphalerite is fragile at relatively low temperatures (<350 °C) (Clark and Kelly, 1973; Couderc et al., 1985; Cox, 1987; Gu et al., 2008; Cugerone et al., 2019). Because the sphalerite particles destroyed by tectonic activities have a larger surface area, the mineral-fluid interaction can proceed completely by the infiltration of late-stage fluids (Gu et al., 2005, 2008). As a result, trace elements with high solubility could be removed from primary sphalerite and highly reconcentrated in other minerals (Kampmann et al., 2018; Cave et al., 2020; Zhao et al., 2021; Ivashchenko, 2021).

Recently, numerous studies suggested that trace elements hosted in sphalerite can be released, when sphalerite-rich orebody suffers from deformation, metamorphism, and fluid overprinting (Jonsson et al., 2013; Kampmann et al., 2018; Carvalho et al., 2018; Bauer et al., 2019b; Cugerone et al., 2020). Carvalho et al. (2018) found that In was highly concentrated in the sphalerite exploited from the tectonically deformed location of the Neves-Corvo deposit, where the concentrations of Cu and In were enhanced by tectonic-metamorphic remobilization. A series of studies conducted by Cugerone et al. (2018, 2019, 2021) have also demonstrated that the tectonic deformation and low-grade metamorphism can remobilize Ge (as well as Cu, Ga, and Sn) from the primary sphalerite, which results in the formation of Ge-minerals in the Pb-Zn deposit of the Variscan Pyrenean Axial Zone. Consequently, trace element remobilization may be a ubiquitous process in sphalerite-rich deposits reworked by late-stage geological processes (George et al., 2016; Reiser et al., 2011; Belissont et al., 2019; Cave et al., 2020). Furthermore, it can be deduced that the trace element characteristics of X-Sp2 are likely controlled by the tectonic deformation.

The LA-ICP-MS maps show that Cu and Sn are highly concentrated in X-Sp2a (Fig. 7h, i) and In is mainly concentrated in X-Sp2b (Fig. 7g). However, higher In concentrations were observed in the relic core of X-Sp2a (Fig. 7g). Considering the high mobility of In during the chemical remobilization process (Shimizu and Morishita, 2012; Bauer et al., 2019b; Zhao et al., 2021), it is possible that In was initially concentrated in X-Sp2a and then reincorporated into X-Sp2b, when the late-stage fluid interacted with the deformed X-Sp2a. This hypothesis was further supported by the BSE images and EMPA maps (Fig. 5h-k and 8). As shown in Fig. 5h-k, the diffused and ragged margin of X-Sp2a indicates a dissolution process (Wu et al., 2019), during which the trace elements in X-Sp2a could be released and subsequently reincorporated into X-Sp2b. Furthermore, high concentrations of Sn and Cu in X-Sp2a, revealed by EMPA maps (Fig. 8), suggest that X-Sp2a could be the source of Sn and Cu for stannite. These stannites, thus, can be regarded as the product of trace element remobilization that occurred in X-Sp2.

The absence of Ga-Cu correlation in X-Sp2a also indicates the remobilization of Ga (Fig. 10A). Because Ga and In were removed from X-Sp2a, the interior correlations between monovalent ions (Cu$^+$ and Ag$^+$) and trivalent ions (Ga^{3+} and In^{3+}) were erased (Fig. 10A), which resulted in the isolation of X-Sp2a relative to other Fe-poor sphalerites (Fig. 9b). In summary, we propose that the early sphalerite generation (X-Sp2a) was first crushed by tectonic activities and then dissolved by late-stage fluids (Fig. 13), which led to the release of trace elements in X-Sp2a. The relatively high solubility of Ga, In, Sn, and Cu would allow them to remain in the fluid during the precipitation of X-Sp2b. Finally, Sn and Cu were locally trapped and concentrated in the microfractures of X-Sp2a, resulting in the formation of stannite. Relatively high availability of Cu, released from X-Sp2a, promotes the incorporations of In and Ga into X-Sp2b.

5.4. Implication for exploration

Understanding the distribution and enrichment mechanism of critical metals in deposits is of both scientific significance and high economic interest (Mondillo et al., 2018b; Torró et al., 2019; Xu et al., 2021a; Xu et al., 2021b). In this study, it can be concluded that the hydrothermal vein-type ores contain more Cd metal than skarn ores in the Chitudian deposit, and the best target for Ga is the orebodies close to the coal beds of the Meiyaogou Formation, especially for the strongly deformed locations. In terms of In, it is generally concentrated in the Fe-rich sphalerite proximal to the hydrothermal feeder (e.g., ore-related granite) (Wu, 2009; Li et al., 2015; Liu et al., 2018; Chen and Zhao, 2021; Yang et al., 2022). Whereas, the present study also stressed that the tectonic deformation, assisted by fluid overprinting, may play an important role in In enrichment (Carvalho et al., 2018; Shimizu and Morishita, 2012; Bauer et al., 2019b). In the Chitudian deposit, four sphalerite-bearing ores from the deformed orebodies give an average In content of 64.4 ppm, which is significantly higher than three undeformed ores (5.40 ppm in average) (the author's unpublished data). These results suggest that the deformed orebodies are ideal exploration targets for In. Since most of the Pb-Zn-Ag deposits in the SNCC are structure-controlled, and multiple-stage deformations and mineralization events have been recognized in these deposits (Gao et al., 2010; Ye, 2006; Li et al., 2013; Li et al., 2016), the Pb-Zn(-Ag) deposits in the SNCC likely have great resource potential for In.

6. Conclusion

(1) Five types of sphalerite were identified in the Chitudian deposit. LA-ICP-MS data suggested that Mn, Fe, In, Cd, Ge, Ga, and Ag are present as solid solutions, whereas Sn, Cu, and Pb occur in solid solutions or microscopic inclusions in these sphalerites.

(2) Critical metals in the Chitudian deposit mainly include Cd, Ga, and In. Cadmium is preferentially concentrated in the sphalerite from the hydrothermal vein-type orebodies. Indium is mostly concentrated in the sphalerite from the granite-proximal orebodies and deformed orebodies. The enrichment of Ga is only found in the sphalerite from the strongly deformed locations of sulfide ore vein, where Ga is derived from the coal beds of the Meiyaogou Formation.

(3) Textural and chemical observations show that trace element remobilization plays a significant role in the enrichment of critical metals in the deformed sphalerite. The sphalerite-rich deposits reworked by late-stage geological events are more potential to explore critical metals.

Conflict of interest statement

We declare that we have no financial and personal relationships with other people or organizations that can inappropriately influence our work, there is no professional or other personal interest of any nature or
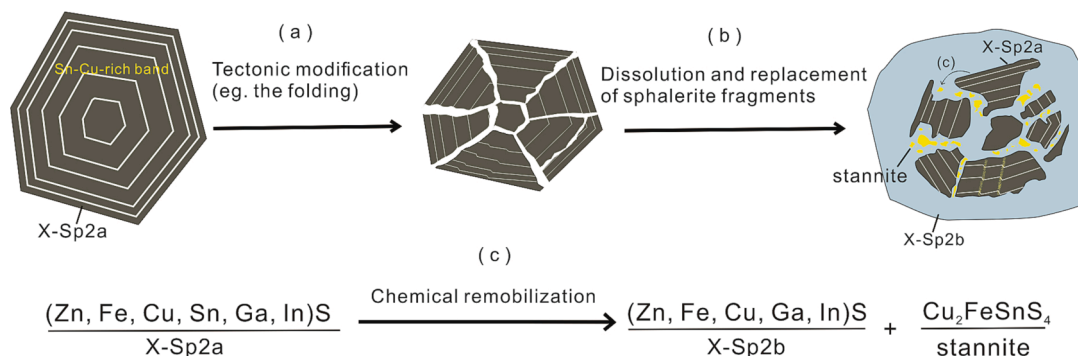
Fig. 13. A sketch model showing the formation processes of X-Sp2.

kind in any product, service and/or company that could be construed as influencing the position.

Declaration of Competing Interest

The authors declare that they have no known competing financial interests or personal relationships that could have appeared to influence the work reported in this paper.

Data availability

I have shared the link to my data at the Attach File step

Appendix A. Supplementary data

Supplementary data to this article can be found online at https://doi.org/10.1016/j.oregeorev.2023.105392.

References

Bao, Z.W., Wang, C.Y., Zhao, T.P., Li, C.J., Gao, X.Y., 2014. Petrogenesis of the Mesozoic granites and Mo mineralization of the Luanchuan ore field in the East Qinling Mo mineralization belt, Central China. Ore Geol. Rev. 57, 132–153.

Bauer, M.E., Burisch, M., Ostendorf, J., Krause, J., Frenzel, M., Seifert, T., Gutzmer, J., 2019a. Trace element geochemistry of sphalerite in contrasting hydrothermal fluid systems of the Freiberg district, Germany: insights from LA-ICP-MS analysis, near-infrared light microthermometry of sphalerite-hosted fluid inclusions, and sulfur isotope geochemistry. Miner. Deposita 54 (2), 237–262.

Bauer, M.E., Seifert, T., Burisch, M., Krause, J., Richter, N., Gutzmer, J., 2019b. Indium-bearing sulfides from the Hämmerlein skarn deposit, Erzgebirge, Germany: evidence for late-stage diffusion of indium into sphalerite. Miner. Deposita 54 (2), 175–192.

Belissont, R., Boiron, M., Luais, B., Cathelineau, M., 2014. LA-ICP-MS analyses of minor and trace elements and bulk Ge isotopes in zoned Ge-rich sphalerites from the Noailhac-Saint-Salvy deposit (France): Insights into incorporation mechanisms and ore deposition processes. Geochim. Cosmochim. Acta 126, 518–540.

Belissont, R., Munoz, M., Boiron, M., Luais, B., Mathon, O., 2019. Germanium Crystal Chemistry in Cu-Bearing Sulfides from Micro-XRF Mapping and Micro-XANES Spectroscopy. Minerals-Basel 9, 227.

Benites, D., Torró, L., Vallance, J., Laurent, O., Valverde, P.E., Kouzmanov, K., Chelle-Michou, C., Fontboté, L., 2021. Distribution of indium, germanium, gallium and other minor and trace elements in polymetallic ores from a porphyry system: The Morococha district. Peru. Ore Geol. Rev. 136.

Cao, H.W., Zhang, S.T., Zheng, G., Liu, R.P., Tian, H.H., Zhang, X.H., Li, J.J., 2013. Geochemical characteristics of trace element of sphalerite in the Zhongyuku Pb-Zn deposit of the Luanchuan, southwest of China. Acta. Mineral. Sin. 33, 1–2 in Chinese.

Cao, H.W., Zhang, S.T., Santosh, M., Zheng, L., Tang, L., Li, D., Zhang, X.H., Zhang, Y.H., 2015. The Luanchuan Mo-W-Pb-Zn-Ag magmatic-hydrothermal system in the East Qinling metallogenic belt, China: Constrains on metallogenesis from C-H-O-S-Pb isotope compositions and Rb-Sr isochron ages. J. Asian Earth Sci. 111, 751–780.

Cao, H.W., Pei, Q.M., Zhang, S.T., Zhang, L.K., Zheng, L., Hu, X.K., 2016. Rb-Sr dating and geological significance of sphalerites from the Zhongyuku Zn(-Pb) deposit in Luanchuan, West Henan, China. J. Chengdu Univ. Technol. 43, 528–538 in Chinese with English abstract.

Carvalho, J.R.S., Relvas, J.M.R.S., Pinto, A.M.M., Frenzel, M., Krause, J., Gutzmer, J., Pacheco, N., Fonseca, R., Santos, S., Caetano, P., Reis, T., Gonçalves, M., 2018. Indium and selenium distribution in the Neves-Corvo deposit, Iberian Pyrite Belt, Portugal. Mineral Mag. 82 (S1), S5–S41.

Cave, B., Lilly, R., Hong, W., 2020. The effect of Co-crystallising sulphides and precipitation mechanisms on sphalerite geochemistry: A case study from the hilton Zn-Pb (Ag) deposit, Australia. Mineral 10, 797.

Chen, T.H., Shi, Q.Z., Shang, Y.Z., Yang, J.F., 1989. Coal resources prediction in Henan Province. Areal Res. Dev. 8, 36–37.

Chen, C., Zhao, T.P., 2021. Metallogenesis of indium in magmatic hydrothermal system. Mineral depos. 40, 206–220 in Chinese with English abstract.

Clark, B.R., Kelly, W.C., 1973. Sulfide Deformation Studies: I. Experimental Deformation of Pyrrhotite and Sphalerite to 2,000 Bars and 500℃. Econ. Geol. 68, 332–352.

Cook, N.J., Ciobanu, C.L., Pring, A., Skinner, W., Shimizu, M., Danyushevsky, L., Saini-Eidukat, B., Melcher, F., 2009. Trace and minor elements in sphalerite: A LA-ICPMS study. Geochim. Cosmochim. Acta 73 (16), 4761–4791.

Cook, N.J., Ciobanu, C.L., Brugger, J., Etschmann, B., Howard, D.L., de Jonge, M.D., Ryan, C., Paterson, D., 2012. Determination of the oxidation state of Cu in substituted Cu-In-Fe-bearing sphalerite via-XANES spectroscopy. Am. Mineral. 97, 476–479.

Couderc, J.J., Dudouit, I., Hennig-Michaeli, C., Levade, C., 1985. The interaction between slip and twinning systems in natural sphalerite experimentally deformed. phys. stat. sol. 90, 581–593.

Cox, S.F., 1987. Flow mechanisms in sulphide minerals. Ore Geol. Rev. 2 (1-3), 133–171.

Cugerone, A., Cenki-Tok, B., Chauvet, A., Le Goff, E., Bailly, L., Alard, O., Allard, M., 2018. Relationships between the occurrence of accessory Ge-minerals and sphalerite in Variscan Pb-Zn deposits of the Bossost anticlinorium, French Pyrenean Axial Zone: Chemistry, microstructures and ore-deposit setting. Ore Geol. Rev. 95, 1–19.

Cugerone, A., Cenki-Tok, B., Oliot, E., Muñoz, M., Barou, F., Motto-Ros, V., Le Goff, E., 2019. Redistribution of germanium during dynamic recrystallization of sphalerite. Geology 48, 236–241.

Cugerone, A., Cenki-Tok, B., Muñoz, M., Kouzmanov, K., Oliot, E., Motto-Ros, V., Le Goff, E., 2020. Behavior of critical metals in metamorphosed Pb-Zn ore deposits: example from the Pyrenean Axial Zone. Miner. Deposita 56 (4), 685–705.

Duan, S.G., Xue, C.J., Chi, G., Liu, G.Y., Yan, C.H., Feng, Q.W., Song, Y.W., 2011. Ore Geology, Fluid Inclusion, and S- and Pb-Isotopic Constraints on the Genesis of the Chitudian Zn-Pb Deposit, Southern Margin of the North China Craton. Resour. Geol. 61, 224–240.

European Commission, Critical Raw Materials. Available online: https://ec.europa.eu/growth/sectors/rawmaterials/specific-interest/critical_en (accessed on 1 April 2019).

Frenzel, M., Ketris, M.P., Gutzmer, J., 2014. On the geological availability of germanium. Miner. Deposita 49 (4), 471–486.

Frenzel, M., Hirsch, T., Gutzmer, J., 2016. Gallium, germanium, indium, and other trace and minor elements in sphalerite as a function of deposit type—A meta-analysis. Ore Geol. Rev. 76, 52–78.

Frenzel, M., Cook, N.J., Ciobanu, C.L., Slattery, A.D., Wade, B.P., Gilbert, S., Ehrig, K., Burisch, M., Verdugo-Ihl, M.R., Voudouris, P., 2020. Halogens in hydrothermal sphalerite record origin of ore-forming fluids. Geology 48, 766–770.

Gao, J.J., Mao, J.W., Ye, H.S., Chen, M.H., Zhang, J.J., Li, Y.F., 2010. Geology and ore-forming fluid of silver-lead-zinc deposit of Shagou, western Henan province. Acta Petrol. Sin. 26, 740–756 in Chinese with English abstract.

Gao, XinYu, Zhao, TaiPing, 2017. Late Mesozoic magmatism and tectonic evolution in the Southern margin of the North China Craton. Sci. China Earth Sci. 60 (11), 1959–1975.

George, L.L., Cook, N.J., Ciobanu, C.L., 2016. Partitioning of trace elements in co-crystallized sphalerite-galena-chalcopyrite hydrothermal ores. Ore Geol. Rev. 77, 97–116.

Gu, X.L., Tang, X.Q., Wang, Z.J., Zheng, Y.C., Wu, C.Z., Lu, J.J., Ni, P., Wu, X.Y., 2005. Sulfide remobilization in NaCl solution at temperature of 362℃ under different stress. Acta Petrol. Sin. 21, 1429–1434 in Chinese with English abstract.

Gu, X.L., Zheng, Y.C., Tang, X.Q., Wang, Z.J., Wu, C.Z., Wu, X.Y., 2008. Remobilization experiments of sulphides under differential stress at 350℃ without addition of external water. Geol. China 35, 1054–1058 in Chinese with English abstract.

Guo, B., Yan, C., Zhang, S., Han, J., Yun, H., Tan, H., Song, Q., Meng, F., Tang, L., 2018. Geochemical and geological characteristics of the granitic batholith and Yuku concealed Mo–W deposit at the southern margin of the North China Craton. Geol. J. 55 (1), 95–116.

He, Y.L., Han, J.W., Yun, H., Hu, H.L., 2020. The discovery of a world-class tungsten and molybdenum ore from deep exploration in Luanchuan molybdenum ore concentrate area. Henan. Geol. China 47, 1934–1936 in Chinese with English abstract.

Ivashchenko, V.I., 2021. Rare-Metal (In, Bi, Te, Se, Be) Mineralization of Skarn Ores in the Pitkäranta Mining District, Ladoga Karelia, Russia. Minerals 11, 124.

Jin, C., Chen, W.T., Gao, X.Y., Li, X.C., Bao, Z.W., Zhao, T.P., 2019. Origin of the Wangpingxigou Pb-Zn deposit in East Qinling orogenic belt, China: Distal response to the giant Donggou porphyry Mo system? Ore Geol. Rev. 109, 101–116.

John, D.A., Taylor, R.D., 2016. By-Products of Porphyry Copper and Molybdenum Deposits. Rev. Econ. Geol. 18, 137–164.

Jonsson, E., Högdahl, K., Majka, J., Lindeberg, T., 2013. Roquesite and associated indium-bearing sulfides from a paleoproterozoic carbonate-hosted mineralization: lindbom's prospect, bergslagen, sweden. The Can. Mineral. 51, 629–641.

Kampmann, T.C., Jansson, N.F., Stephens, M.B., Olin, P.H., Gilbert, S., Wanhainen, C., 2018. Syn-tectonic sulphide remobilization and trace element redistribution at the Falun pyritic Zn-Pb-Cu-(Au-Ag) sulphide deposit, Bergslagen. Sweden. Ore Geol. Rev. 96, 48–71.

Koch, I., 2012. Analysis of multivariate and high-dimensional data theory and prectice. Cambridge University Press, Cambridge.

Lee, J.H., Yoo, B.C., Yang, Y.S., Lee, T.H., Seo, J.H., 2019. Sphalerite geochemistry of the Zn-Pb orebodies in the Taebaeksan metallogenic province. Korea. Ore Geol. Rev. 107, 1046–1067.

Li, J.J., 2014. Structure characteristics of Luanchuan ore-concentrated area and its ore-controlling function (Master degree thesis). China University of Geosciences, Beijing. 1–66 in Chinese with English abstract.

Li, D., Han, J.W., Zhang, S.T., Yan, C.H., Cao, H.W., Song, Y.W., 2015. Temporal evolution of granitic magmas in the Luanchuan metallogenic belt, east Qinling Orogen, central China: Implications for Mo metallogenesis. J. Asian Earth Sci. 111, 663–680.

Li, Z.K., Li, J.W., Zhao, X.F., Zhou, M.F., Selby, D., Bi, S.J., Sui, J.X., Zhao, Z.J., 2013. Crustal-Extension Ag-Pb-Zn Veins in the Xiong'ershan District, Southern North China: Constraints from the Shagou Deposit. Econ. Geol. 108, 1703–1729.

Li, Z.K., Li, J.W., Cooke, D.R., Danyushevsky, L., Zhang, L.J., Brien, O.H, Lahaye, Y., Zhang, W., Xu, H.J., 2016. Textures, trace elements, and Pb isotopes of sulfides from the Haopinggou vein deposit, southern North China Craton: implications for discrete Au and Ag-Pb-Zn mineralization. Contrib. Miner. Petrol. 171, 99.

Li, Z.K., Bi, S.J., Li, J.W., Zhang, W., Cooke, D.R., Selby, D., 2017. Distal Pb-Zn-Ag veins associated with the world-class Donggou porphyry Mo deposit, southern North China craton. Ore Geol. Rev. 82, 232–251.

Liu, Y.S., Hu, Z.C., Gao, S., Günther, D., Xu, J., Gao, C.G., Chen, H.H., 2008. In situ analysis of major and trace elements of anhydrous minerals by LA-ICP-MS without applying an internal standard. Chem. Geol. 257, 34–43.

Liu, J.P., Rong, Y.Y., Gu, X.P., Shao, Y.J., Lai, J.Q., Chen, W.K., 2018. Indium Mineralization in the Yejiwei Sn-Polymetallic Deposit of the Shizhuyuan Orefield, Southern Hunan. China. Resour. Geol. 68, 22–36.

Mao, J.W., Ye, H.S., Wang, R.Y., Dai, J.Z., Jian, W., Xiang, J.F., Zhou, K., Meng, F., 2009. Mineral deposit model of Mesozoic porphyry Mo and vein-type Pb-Zn-Ag ore deposits in the eastern Qinling, Central China and its implication for prospecting. Geol. Bull. China 28, 72–79 in Chinese with English abstract.

Mao, J.W., Pirajno, F., Xiang, J.F., Gao, J.J., Ye, H.S., Li, Y.F., Guo, B.J., 2011. Mesozoic molybdenum deposits in the east Qinling-Dabie orogenic belt: Characteristics and tectonic settings. Ore Geol. Rev. 43, 264–293.

Mondillo, N., Arfè, G., Herrington, R., Boni, M., Wilkinson, C., Mormone, A., 2018a. Germanium enrichment in supergene settings: evidence from the Cristal nonsulfide Zn prospect, Bongará district, northern Peru. Miner. Deposita 53, 155–169.

Mondillo, N., Herrington, R., Boyce, A.J., Wilkinson, C., Santoro, L., Rumsey, M., 2018b. Critical elements in non-sulfide Zn deposits: a reanalysis of the Kabwe Zn-Pb ores (central Zambia). Mineral. Mag. 82, S89–S114.

Murakami, H., Ishihara, S., 2013. Trace elements of Indium-bearing sphalerite from tin-polymetallic deposits in Bolivia, China and Japan: A femto-second LA-ICPMS study. Ore Geol. Rev. 53, 223–243.

Ning, S.Y., Wang, F.Y., Xue, W.D., Zhou, T.F., 2017. Geochemistry of the Baoshan pluton in the Tongling region of the Lower Yangtze River Belt. Geochimica 46, 397–412 in Chinese with English abstract.

Oyebamiji, A., Hu, R.Z., Zhao, C.H., Zafar, T., 2020. Origin of the Triassic Qilinchang Pb-Zn deposit in the western Yangtze block, SW China: Insights from in-situ trace elemental compositions of base metal sulphides. J. Asian Earth Sci. 192, 104292.

Reiser, F.K.M., Rosa, D.R.N., Pinto, Á.M.M., Carvalho, J.R.S., Matos, J.X., Guimarães, F. M.G., Alves, L.C., De Oliveira, D.P.S., 2011. Mineralogy and geochemistry of tin- and germanium-bearing copper ore, Barrigão re-mobilized vein deposit, Iberian Pyrite Belt. Portugal. Int. Geol, Rev, p. 53.

Rudnick, R.L., Gao, S., 2014. 4.1 - Composition of the Continental Crust. In: Holland, H. D., Turekian, K.K. (Eds.), Treatise on Geochemistry (Second Edition), Oxford. Elsevier, pp. 1–51.

Sahlström, F., Arribas, A., Dirks, P., Corral, I., Chang, Z., 2017. Mineralogical Distribution of Germanium, Gallium and Indium at the Mt Carlton High-Sulfidation Epithermal Deposit, NE Australia, and Comparison with Similar Deposits Worldwide. Minerals (Basel) 7, 213.

Schwartz, M.O., 2000. Cadmium in zinc deposits: Economic geology of a polluting element. Int. Geol. Rev. 42, 445–469.

Shang, J., Lu, J.W., Peng, X.L., Zhang, Y., 2007. Mineragraphy. Geological Publishing House, Beijing.

Shimizu, T., Morishita, Y., 2012. Petrography, chemistry, and near-infrared microthermometry of indium-bearing sphalerite from the toyoha polymetallic deposit. Japan. Econ. Geol. 107, 723–735.

Stergiou, C.L., Melfos, V., Voudouris, P., Papadopoulou, L., Spry, P.G., Peytcheva, I., Dimitrova, D., Stefanova, E., Giouri, K., 2021. Rare and critical metals in pyrite, chalcopyrite, magnetite, and titanite from the vathi porphyry Cu-Au±Mo deposit, Northern Greece. Minerals 11, 630.

Tian, H.H., Zhang, S.T., Cao, H.W., Han, J.W., Lv, P.D., Zhang, Y.H., 2015. Geochemical characteristics of trace elements of sphalerite in the Chitudian Pb- Zn deposit, West Henan Province. Bulletin of Mineralogy. Petrol. Ceocherm. 34, 334–342 in Chinese with English abstract.

Torró, L., Melgarejo, J., Gemmrich, L., Mollinedo, D., Cazorla, M., Martínez, Á., Pujol-Solà, N., Farré-de-Pablo, J., Camprubí, A., Artiaga, D., Torres, B., Alfonso, P., Arce, O., 2019. Spatial and Temporal Controls on the Distribution of Indium in Xenothermal Vein-Deposits: The Huari Huari District, Potosí. Bolivia. Minerals-Basel 9, 304.

Tu, G.C., 2004. The Geochemistry and Ore-Forming Mechanism of the Dispersed Elements. Geological Publishing House, Beijing, pp. 1–424 in Chinese.

Wang, F.Y., Ge, C., Ning, S.Y., Nie, L.Q., Zhong, G.X., White, N.C., 2017. A new approach to LA-ICP-MS mapping and application in geology. Acta Petrol. Sin. 33, 3422–3436 in Chinese with English abstract.

Wang, S., Zhang, Y., Zhang, H., Zhu, A.M., Wang, H.M., Shi, X.F., Ye, H.S., Yang, Y.Q., 2018. Petrogenesis and tectonic setting of the Mesozoic Huoshenmiao intrusion in the Luanchuan ore district, Henan Province. North China. J. Asian Earth Sci. 160, 239–257.

Wang, G.W., Zhang, S.T., Yan, C.H., Pang, Z.S., Wang, H.W., Feng, Z.K., Dong, H., Cheng, H.T., He, Y.Q., Li, R.X., Zhang, Z.Q., Huang, L.L., Guo, N.N., 2021. Resource environmental joint forecasting in the Luanchuan mining district, China through big data mining and 3D/4D modeling. Earth Sci. Front. 28, 139–155.

Wei, C., Huang, Z.L., Yan, Z.F., Hu, Y.S., Ye, L., 2018. Trace element contents in sphalerite from the nayongzhi zn-pb deposit, Northwestern Guizhou, China: insights into incorporation mechanisms, metallogenic temperature and ore genesis. Minerals-Basel 8, 490.

Wei, C., Ye, L., Hu, Y.S., Danyushevskiy, L., Li, Z.L., Huang, Z.L., 2019. Distribution and occurrence of Ge and related trace elements in sphalerite from the Lehong carbonate-hosted Zn-Pb deposit, northeastern Yunnan, China: Insights from SEM and LA-ICP-MS studies. Ore Geol. Rev. 115.

Wei, C., Ye, L., Hu, Y.S., Huang, Z.L., Danyushevsky, L., Wang, H.Y., 2021. LA-ICP-MS analyses of trace elements in base metal sulfides from carbonate-hosted Zn-Pb deposits, South China: A case study of the Maoping deposit. Ore Geol. Rev. 130, 103945.

Wen, H.J., Zhu, C.W., Zhang, Y.X., Cloquet, C., Fan, H.F., Fu, S.H., 2016. Zn/Cd ratios and cadmium isotope evidence for the classification of lead-zinc deposits. Sci. Rep. 6, 25273.

Wen, H.J., Zhou, Z.B., Zhu, C.W., Luo, C.G., Wang, D.Z., Du, S.J., Li, X.F., 2019. Chen MH and Li HY. 2019. Critical scientific issues ofsuper-enrichment of dispersed metals. Acta Petrol. Sin. 35, 3271–3291 in Chinese with English abstract.

Werner, T.T., Mudd, G.M., Jowitt, S.M., 2017. The world's by-product and critical metal resources part III: A global assessment of indium. Ore Geol. Rev. 86, 939–956.

Wu, Y.T., 2009. Study on the enrichment regularity of indium in Dachang ore-field, Guangxi. Central South University, Changsha, pp. 1–145 (P.hd thesis). (in Chinese with English abstract.

Wu, Y.F., Evans, K., Li, J.E., Fougerouse, D., Large, R.R., Guagliardo, P., 2019. Metal remobilization and ore-fluid perturbation during episodic replacement of auriferous pyrite from an epizonal orogenic gold deposit. Geochim. Cosmochim. Acta 245, 98–117.

Xiao, X., Zhou, T.F., White, N.C., Zhang, L.J., Fan, Y., Wang, F.Y., Chen, X.F., 2018. The formation and trace elements of garnet in the skarn zone from the Xinqiao Cu-S-Fe-Au deposit, Tongling ore district, Anhui Province, Eastern China. Lithos 302–303, 467–479.

Xing, B., Xiang, J.F., Ye, H.S., Chen, X.D., Zhang, G.S., Yang, C.Y., Jin, X., Hu, Z.Z., 2017. Genesis of Luotuoshan sulfur polymetallic deposit in western Henan Province: Evidence from trace elements of sulfide revealed by using LA-ICP-MS in lamellar ores. Mineral Depos. 36, 83–106 in Chinese with English abstract.

Xing, B., Mao, J.W., Xiao, X.N., Liu, H., Jia, F.D., Wang, S.S., Huang, W.Y., Li, H.Y., 2021. Genetic discrimination of the Dingjiashan Pb-Zn deposit, SE China, based on sphalerite chemistry. Ore Geol. Rev. 135.

Xu, T., 2015. Characteristics of Ore-forming Fluid and Significance of Prospecting of Luotuoshan Sulphur Polymetallic Deposit in Luanchuan, Western Henan (Master degree thesis). China Univ. Geosci., Beijing. 1–46 in Chinese with English abstract.

Xu, J., Cook, N.J., Ciobanu, C.L., Li, X.F., Kontonikas-Charos, A., Gilbert, S., Lv, Y.H., 2021a. Indium distribution in sphalerite from sulfide-oxide-silicate skarn assemblages: a case study of the Dulong Zn-Sn-In deposit, Southwest China. Miner. Deposita 56, 307–324.

Xu, J., Ciobanu, C.L., Cook, N.J., Slattery, A., Li, X.F., Kontonikas-Charos, A., 2021b. Phase relationships in the system ZnS-CuInS2: Insights from a nanoscale study of indium-bearing sphalerite. Am. Mineral. 106, 192–205.

Xu, X.S., Griffin, W.L., Ma, X., Reilly, O., He, Z.Y., Zhang, C.L., 2009. The Taihua group on the southern margin of the North China craton: further insights from U-Pb ages and Hf isotope compositions of zircons. Miner. Petrol. 97, 43–59.

Xue, F., Wang, G.W., Santosh, M., Yang, F., Shen, Z.W., Kong, L., Guo, N.N., Zhang, X.H., Jia, W.J., 2018. Geochemistry and geochronology of ore-bearing and barren

intrusions in the Luanchuan ore fields of East Qinling metallogenic belt, China: Diverse tectonic evolution and implications for mineral exploration. J. Asian Earth Sci. 157, 57–77.

Yang, X., Li, Y.Q., Chen, J.H., 2022. DFT study of the occurrence state of In and the correlation of In and Fe in sphalerite. Miner. Eng. 183, 107596.

Yang, F., Wang, G., Cao, H., Li, R., Tang, L.i., Huang, Y., Zhang, H., Xue, F., Jia, W., Guo, N., 2017a. Timing of formation of the Hongdonggou Pb-Zn polymetallic ore deposit, Henan Province, China: Evidence from Rb-Sr isotopic dating of sphalerites. Geosci. Front. 8 (3), 605–616.

Yang, F., Wang, G.W., Santosh, M., Li, R.X., Tang, L., Cao, H.W., Guo, N.N., Liu, C., 2017b. Delineation of potential exploration targets based on 3D geological modeling: A case study from the Laoangou Pb-Zn-Ag polymetallic ore deposit. China. Ore Geol. Rev. 89, 228–252.

Ye, H.S., 2006. The Mesozoic Tectonic Evolution and Pb-Zn-Ag Metallogeny in the South Margin of North China Craton. China University of Geosciences, Beijing, pp. 1–217 (Ph.D. thesis).(in Chinese with English abstract.

Ye, L., Cook, N.J., Ciobanu, C.L., Liu, Y., Zhang, Q., Liu, T.G., Gao, W., Yang, Y.L., Leonid, D., 2011. Trace and minor elements in sphalerite from base metal deposits in South China: A LA-ICPMS study. Ore Geol. Rev. 39, 188–217.

Yin, X.Z., Hu, A.Z., 2004. A tentative discussion on the genesis of some Pb-Zn deposits in western Henan based on typomorphic characteristics of sphalerite. Geophys. Geochem. Explor. 28, 413–414 in Chinese with English abstract.

Yuan, B., Zhang, C.Q., Yu, H.J., Yang, Y.M., Zhao, Y.X., Zhu, C.C., Ding, Q.F., Zhou, Y.B., Yang, J.C., Xu, Y., 2018. Element enrichment characteristics: Insights from element geochemistry of sphalerite in Daliangzi Pb–Zn deposit, Sichuan, Southwest China. J. Geochem. Explor. 186, 187–201.

Zhang, Q., 1987. Trace elements in galena and sphalerite and their geochemical significance in distinguishing the genetic types of Pb-Zn ore deposits. Chin. J. Geochem. 6, 177–190.

Zhang, Y.H., Cao, H.W., Xu, M., Zhang, S.T., Tang, L., Wang, S.Y., Pei, Q.M., Cai, G.J., Shen, T., 2018. Petrogenesis of the late Mesozoic highly fractionated I-type granites in the Luanchuan ore district: implications for the tectono-magmatic evolution of eastern Qinling. Geosci. J. 22, 253–272.

Zhang, G.W., Guo, A.L., Liu, F.T., Xiao, Q.H., Meng, Q.R., 1996. Three-dimensional architecture and dynamic analysis of the Qinling orogenic belt. Sci China Ser D-Earth Sci 26, 1–6.

Zhang, Z.Q., Wang, G.W., Ma, Z.B., Carranza, E.J.M., Jia, W.J., Du, J.G., Tao, G.S., Deng, Z.P., 2019. Batholith-stock scale exploration targeting based on multi-source geological and geophysical datasets in the Luanchuan Mo polymetallic district. China. Ore Geol. Rev. 118, 103225.

Zhang, Q., Zhan, X.Z., Pan, J.Y., Shao, S.X., 1998. Geochemical Enrichment and Mineralization of Indium. Chin. J. Geochem. 17, 221–225.

Zhao, T.P., Zhai, M.G., Xia, B., Li, H.M., Zhang, Y.X., Wan, Y.S., 2004. Zircon U-Pb SHRIMP dating for the volcanic rocks of the Xiong'er Group: Constraints on the initial formation age of the cover of the North China Craton. Chin. Sci. Bull. 49, 2495–2502.

Zhao, T.P., Meng, L., Gao, X.Y., Jin, C., Wu, Q., Bao, Z.W., 2018. Late Mesozoic felsic magmatism and Mo-Au-Pb-Zn mineralization in the southern margin of the North China Craton: A review. J. Asian Earth Sci. 161, 103–121.

Zhao, T.P., Chen, C., He, X.H., Meng, L., Xu, J., Liu, W.Y., 2022. A synthesis of the geology, spatial–temporal distribution and enrichment mechanism of granite-related indium deposits in China. Ore Geol. Rev. 146, 104932.

Zhao, Z.X., Wei, J.H., Liang, S.N., Gao, T., 2021. Sulfide remobilization and trace element redistribution during metamorphism and deformation at the Xitieshan Pb-Zn deposit, NW China. Ore Geol. Rev. 134, 104170.

Zhou, Z.B., Wen, H.J., 2021. A magmatic-hydrothermal indium-bearing polymetallic vein mineralization belt in the western Jiangnan Orogen: Evidence from zinc and cadmium isotopes of sphalerite. Ore Geol. Rev. 131, 103843.

Zhuang, L.L., Song, Y.C., Liu, Y.C., Fard, M., Hou, Z.Q., 2019. Major and trace elements and sulfur isotopes in two stages of sphalerite from the world-class Angouran Zn-Pb deposit, Iran: Implications for mineralization conditions and type. Ore Geol. Rev. 109, 184–200.

Zuo, P.F., 2016. Meso-Neoproterozoic to Early Paleozoic Tectonics and Mineralization of Black Shales in Southwest Henan, China. China University of Geosciences, Beijing, pp. 1–174 (Ph.D. thesis).(in Chinese with English abstract.